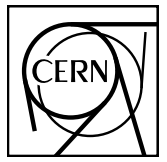


# EUROPEAN ORGANIZATION FOR NUCLEAR RESEARCH



ALICE-ANA-2016-xxx  
June 7, 2017

## Lambda-Kaon and Cascade-Kaon Femtoscopy in Pb-Pb Collisions at $\sqrt{s_{NN}} = 2.76$ TeV from the LHC ALICE Experiment

Jesse T. Buxton<sup>1</sup>

1. Department of Physics, The Ohio State University, Columbus, Ohio, USA

Email: jesse.thomas.buxton@cern.ch

### Abstract

We present results from a femtoscopic analysis of Lambda-Kaon correlations in Pb-Pb collisions at  $\sqrt{s_{NN}} = 2.76$  TeV by the ALICE experiment at the LHC. All pair combinations of  $\Lambda$  and  $\bar{\Lambda}$  with  $K^+$ ,  $K^-$  and  $K_S^0$  are analyzed. The femtoscopic correlations are the result of strong final-state interactions, and are fit with a parametrization based on a model by R. Lednicky and V. L. Lyuboshitz [1]. This allows us to both characterize the emission source and measure the scattering parameters for the particle pairs. We observe a large difference in the  $\Lambda$ - $K^+$  ( $\bar{\Lambda}$ - $K^-$ ) and  $\Lambda$ - $K^-$  ( $\bar{\Lambda}$ - $K^+$ ) correlations in pairs with low relative momenta ( $k^* \lesssim 100$  MeV). Additionally, the average of the  $\Lambda$ - $K^+$  ( $\bar{\Lambda}$ - $K^-$ ) and  $\Lambda$ - $K^-$  ( $\bar{\Lambda}$ - $K^+$ ) correlation functions is consistent with our  $\Lambda$ - $K_S^0$  ( $\bar{\Lambda}$ - $K_S^0$ ) measurement. The results suggest an effect arising from different quark-antiquark interactions in the pairs, i.e.  $s\bar{s}$  in  $\Lambda$ - $K^+$  ( $\bar{\Lambda}$ - $K^-$ ) and  $u\bar{u}$  in  $\Lambda$ - $K^-$  ( $\bar{\Lambda}$ - $K^+$ ). To gain further insight into this hypothesis, we currently are conducting a  $\Xi$ -K femtoscopic analysis.



## Contents

<b>1</b>	<b>Introduction</b>	<b>4</b>
<b>2</b>	<b>Data Sample and Software</b>	<b>4</b>
2.1	Data Sample . . . . .	4
2.2	Software . . . . .	4
<b>3</b>	<b>Data Selection</b>	<b>5</b>
3.1	Event Selection and Mixing . . . . .	5
3.2	K $^{\pm}$ Track Selection . . . . .	5
3.3	V0 Selection . . . . .	7
3.3.1	Λ Reconstruction . . . . .	7
3.3.2	K $_S^0$ Reconstruction . . . . .	9
3.4	Cascade Reconstruction . . . . .	12
3.5	Pair Selection . . . . .	14
<b>4</b>	<b>Correlation Functions</b>	<b>15</b>
<b>5</b>	<b>Fitting</b>	<b>16</b>
5.1	Model: ΛK $_S^0$ , ΛK $^{\pm}$ , Ξ $^{ch}$ K $_S^0$ . . . . .	16
5.2	Model: Ξ $^{ch}$ K $^{ch}$ . . . . .	19
5.3	Momentum Resolution Corrections . . . . .	22
5.4	Residual Correlations . . . . .	23
<b>6</b>	<b>Systematic Errors</b>	<b>26</b>
6.1	Systematic Errors: ΛK $_S^0$ . . . . .	27
6.1.1	Particle and Pair Cuts . . . . .	27
6.1.2	Non-Flat Background . . . . .	28
6.1.3	Fit Range . . . . .	28
6.2	Systematic Errors: ΛK $^{\pm}$ . . . . .	28
6.2.1	Particle and Pair Cuts . . . . .	28
6.2.2	Non-Flat Background . . . . .	28
6.2.3	Fit Range . . . . .	28
6.3	Systematic Errors: ΞK $^{\pm}$ . . . . .	29
6.3.1	Particle and Pair Cuts . . . . .	29

<b>7 Results and Discussion</b>	<b>29</b>
7.1 Results: $\Lambda K_S^0$ and $\Lambda K^\pm$ . . . . .	29
7.2 Results: $\Xi K^\pm$ . . . . .	38
<b>8 To Do</b>	<b>40</b>

## List of Figures

1	V0 Reconstruction	7
2	$K_S^0$ contamination in $\Lambda(\bar{\Lambda})$ collection	9
3	$\Lambda$ and $\bar{\Lambda}$ Purity	9
4	$\Lambda(\bar{\Lambda})$ contamination in $K_S^0$ collection	11
5	$K_S^0$ Purity	12
6	$\Xi$ Reconstruction	13
7	$\Xi^-(\bar{\Xi}^+)$ Purity	14
8	Average Separation of $\Lambda(\bar{\Lambda})$ and $K_S^0$ Daughters	15
9	Average Separation of $\Lambda(\bar{\Lambda})$ Daughter and $K^\pm$	16
10	Average Separation of $\Xi$ Daughters and $K^\pm$	17
11	$\Lambda(\bar{\Lambda})K_S^0$ Correlation Functions	18
12	$\Lambda K^+$ and $\bar{\Lambda} K^-$ Correlation Functions	19
13	$\Lambda K^-$ and $\bar{\Lambda} K^+$ Correlation Functions	20
14	Correlation Functions: $\Lambda K^+$ vs $\Lambda K^-$ for 0-10% Centrality	21
15	Momentum Resolution: Sample $k_{True}^*$ vs. $k_{Rec}^*$	24
16	Particle Contaminations Visible in $k_{True}^*$ vs. $k_{Rec}^*$	25
17	Transform Matrices for $\Lambda K^+$ Analysis	26
18	Transform Matrices for $\bar{\Lambda} K^+$ Analysis	27
19	$\Lambda K_S^0(\bar{\Lambda} K_S^0)$ Fits	30
20	$\Lambda K_S^0(\bar{\Lambda} K_S^0)$ Fits (Wide Range)	31
21	$\Lambda K^+(\bar{\Lambda} K^-)$ Fits	32
22	$\Lambda K^+(\bar{\Lambda} K^-)$ Fits (Wide Range)	33
23	$\Lambda K^-(\bar{\Lambda} K^+)$ Fits	34
24	$\Lambda K^-(\bar{\Lambda} K^+)$ Fits (Wide Range)	35
25	$m_T$ Scaling of Radii	38
26	$\Xi K^\pm$ Results	38
27	$\Xi K^\pm$ Data with Coulomb-Only Bands, 0-10% Centrality	39
28	Effect of Strong Force Inclusion on Coulomb-Only Curve for $\Xi K^\pm$ systems	41
29	$\Xi K^\pm$ Global Coulomb-Only Fit (Set 1)	42
30	$\Xi K^\pm$ Global Coulomb-Only Fit (Set 2)	43
31	$\Xi^- K^+$ Coulomb-Only Fit	43
32	$\Xi^- K^-$ Coulomb-Only Fit	44

---

## 12 1 Introduction

13 NOTE: An updated version of this analysis note should be uploaded before 16 December 2016. Amongst  
 14 other additions, this new version will include more thorough results and discussion of our  $\Xi K^\pm$  analyses.  
 15 If possible, we would like to at least show the data from this study, and possibly even preliminary results.  
 16 However, with QM deadlines close approaching, this may not be possible.

17 We present results from a femtoscopic analysis of Lambda-Kaon correlations in Pb-Pb collisions at  $\sqrt{s_{NN}}$   
 18 = 2.76 TeV by the ALICE experiment at the LHC. All pair combinations of  $\Lambda$  and  $\bar{\Lambda}$  with  $K^+$ ,  $K^-$  and  
 19  $K_S^0$  are analyzed. The femtoscopic correlations are the result of strong final-state interactions, and are  
 20 fit with a parametrization based on a model by R. Lednický and V. L. Lyuboshitz [1]. This allows us to  
 21 both characterize the emission source and measure the scattering parameters for the particle pairs. We  
 22 observe a large difference in the  $\Lambda$ - $K^+$  ( $\bar{\Lambda}$ - $K^-$ ) and  $\Lambda$ - $K^-$  ( $\bar{\Lambda}$ - $K^+$ ) correlations in pairs with low relative  
 23 momenta ( $k^* \lesssim 100$  MeV). Additionally, the average of the  $\Lambda$ - $K^+$  ( $\bar{\Lambda}$ - $K^-$ ) and  $\Lambda$ - $K^-$  ( $\bar{\Lambda}$ - $K^+$ ) correlation  
 24 functions is consistent with our  $\Lambda$ - $K_S^0$  ( $\bar{\Lambda}$ - $K_S^0$ ) measurement. The results suggest an effect arising from  
 25 different quark-antiquark interactions in the pairs, i.e.  $s\bar{s}$  in  $\Lambda$ - $K^+$  ( $\bar{\Lambda}$ - $K^-$ ) and  $u\bar{u}$  in  $\Lambda$ - $K^-$  ( $\bar{\Lambda}$ - $K^+$ ). To  
 26 gain further insight into this hypothesis, we currently are conducting a  $\Xi$ - $K$  femtoscopic analysis.

## 27 2 Data Sample and Software

### 28 2.1 Data Sample

29 The analysis used “pass 2” reconstructed Pb-Pb data from LHC11h (AOD145). The runlist was selected  
 30 from runs with global quality tag “1” in the ALICE Run Condition Table. Approximately 40 million  
 31 combined central, semi-central, and minimum bias events were analyzed. Runs from both positive (++)  
 32 and negative (--) magnetic field polarity settings were used.

33 Run list: 170593, 170572, 170388, 170387, 170315, 170313, 170312, 170311, 170309, 170308, 170306,  
 34 170270, 170269, 170268, 170230, 170228, 170207, 170204, 170203, 170193, 170163, 170159, 170155,  
 35 170091, 170089, 170088, 170085, 170084, 170083, 170081, 170040, 170027, 169965, 169923, 169859,  
 36 169858, 169855, 169846, 169838, 169837, 169835, 169591, 169590, 169588, 169587, 169586, 169557,  
 37 169555, 169554, 169553, 169550, 169515, 169512, 169506, 169504, 169498, 169475, 169420, 169419,  
 38 169418, 169417, 169415, 169411, 169238, 169167, 169160, 169156, 169148, 169145, 169144, 169138,  
 39 169099, 169094, 169091, 169045, 169044, 169040, 169035, 168992, 168988, 168826, 168777, 168514,  
 40 168512, 168511, 168467, 168464, 168460, 168458, 168362, 168361, 168342, 168341, 168325, 168322,  
 41 168311, 168310, 168115, 168108, 168107, 168105, 168076, 168069, 167988, 167987, 167985, 167920,  
 42 167915

43 Analysis was also performed on the LHC12a17a\_fix (AOD149) Monte Carlo HIJING events for certain  
 44 checks. THERMINATOR2 was also used for certain aspects, such as transform matrices described feed-  
 45 down contributions.

### 46 2.2 Software

47 The analysis was performed on the PWGCF analysis train using AliRoot v5-08-18-1 and AliPhysics  
 48 vAN-20161027-1.

49 The main classes utilized include: AliFemtoVertexMultAnalysis, AliFemtoEventCutEstimators, AliFem-  
 50 toESDTrackCutNSigmaFilter, AliFemtoV0TrackCutNSigmaFilter, AliFemtoXiTrackCut, AliFemtoV0PairCut,  
 51 AliFemtoV0TrackPairCut, AliFemtoXiTrackPairCut, and AliFemtoAnalysisLambdaKaon. All of these  
 52 classes are contained in /AliPhysics/PWGCF/FEMTOSCOPY/AliFemto and .../AliFemtoUser.

53    **3 Data Selection**

54    **3.1 Event Selection and Mixing**

55    The events used in this study were selected with the class AliFemtoEventCutEstimators according to the  
 56    following criteria:

- 57        – Triggers
  - 58            – minimum bias (kMB)
  - 59            – central (kCentral)
  - 60            – semi-central (kSemiCentral)
- 61        – z-position of reconstructed event vertex must be within 10 cm of the center of the ALICE detector
- 62        – the event must contain at least one particle of each type from the pair of interest

63    The event mixing was handled by the AliFemtoVertexMultAnalysis class, which only mixes events with  
 64    like vertex position and centrality. The following criteria were used for event mixing:

- 65        – Number of events to mix = 5
- 66        – Vertex position bin width = 2 cm
- 67        – Centrality bin width = 5

68    The AliFemtoEventReaderAODChain class is used to read the events. Event flattening is not currently  
 69    used. FilterBit(7). The centrality is determined by the “V0M” method of AliCentrality, set by calling Al-  
 70    iFemtoEventReaderAOD::SetUseMultiplicity(kCentrality). I utilize the SetPrimaryVertexCorrectionT-  
 71    PCPoints switch, which causes the reader to shift all TPC points to be relative to the event vertex.

72    **3.2  $K^\pm$  Track Selection**

73    Charged kaons are identified using the AliFemtoESDTrackCutNSigmaFilter class. The specific cuts used  
 74    in this analysis are as follows:

75    Track Selection:

- 76        – Kinematic range:
  - 77            –  $0.14 < p_T < 1.5$
  - 78            –  $|\eta| < 0.8$
- 79        – FilterBit(7)
  - 80            – TPC tracks
- 81        – Track Quality
  - 82            – Minimum number of clusters in the TPC (fminTPCncls) = 80
  - 83            – Maximum allowed  $\chi^2/N_{DOF}$  for ITS clusters = 3.0
  - 84            – Maximum allowed  $\chi^2/N_{DOF}$  for TPC clusters = 4.0
- 85        – Primary Particle Selection:

- 86        – Maximum XY impact parameter = 2.4
- 87        – Maximum Z impact parameter = 3.0
- 88        – Remove particles with any kink labels (fRemoveKinks = true)
- 89        – Maximum allowed sigma to primary vertex (fMaxSigmaToVertex) = 3.0

90 K $^\pm$  Identification:

- 91        – PID Probabilities:

- 92            – K: > 0.2
- 93            –  $\pi$ : < 0.1
- 94            –  $\mu$ : < 0.8
- 95            – p: < 0.1

- 96        – Most probable particle type must be Kaon (fMostProbable=3)

- 97        – TPC and TOF N $_\sigma$  cuts:

- 98            – p < 0.4 GeV/c: N $_{\sigma K,TPC}$  < 2
- 99            – 0.4 < p < 0.45 GeV/c: N $_{\sigma K,TPC}$  < 1
- 100          – 0.45 < p < 0.8 GeV/c: N $_{\sigma K,TPC}$  < 3 & N $_{\sigma K,TOF}$  < 2
- 101          – 0.8 < p < 1.0 GeV/c: N $_{\sigma K,TPC}$  < 3 & N $_{\sigma K,TOF}$  < 1.5
- 102          – p > 1.0 GeV/c: N $_{\sigma K,TPC}$  < 3 & N $_{\sigma K,TOF}$  < 1

- 103        – Electron Rejection: Reject if N $_{\sigma e-,TPC}$  < 3

- 104        – Pion Rejection: Reject if:

- 105            – p < 0.65
  - 106              \* if TOF and TPC available: N $_{\sigma \pi,TPC}$  < 3 & N $_{\sigma \pi,TOF}$  < 3
  - 107              \* else
    - 108                · p < 0.5: N $_{\sigma \pi,TPC}$  < 3
    - 109                · 0.5 < p < 0.65: N $_{\sigma \pi,TPC}$  < 2
- 110            – 0.65 < p < 1.5: N $_{\sigma \pi,TPC}$  < 5 & N $_{\sigma \pi,TOF}$  < 3
- 111            – p > 1.5: N $_{\sigma \pi,TPC}$  < 5 & N $_{\sigma \pi,TOF}$  < 2

112 The purity of the K $^\pm$  collections was estimated using the MC data, for which the true identity of each  
 113 reconstructed K $^\pm$  particle is known. Therefore, the purity may be estimated as:

$$\text{Purity}(K^\pm) = \frac{N_{\text{true}}}{N_{\text{reconstructed}}} \quad (1)$$

114 Purity(K $^+$ )  $\approx$  Purity(K $^-$ )  $\approx$  97%

115 **3.3 V0 Selection**

116  $\Lambda$  ( $\bar{\Lambda}$ ) and  $K_S^0$  are neutral particles which cannot be directly detected, but must instead be reconstructed  
 117 through detection of their decay products, or daughters. This process is illustrated in Figure 1. In  
 118 general, particles which are topologically reconstructed in this fashion are called V0 particles. The  
 119 class AliFemtoV0TrackCutNSigmaFilter (which is an extension of AliFemtoV0TrackCut) is used to  
 120 reconstruct the V0s.

121 In order to obtain a true and reliable signal, one must ensure good purity of the V0 collection. The purity  
 122 of the collection is calculated as:

$$\text{Purity} = \frac{\text{Signal}}{\text{Signal} + \text{Background}} \quad (2)$$

123 To obtain both the signal and background, the invariant mass distribution ( $m_{inv}$ ) of all V0 candidates  
 124 must be constructed immediately before the final invariant mass cut. Examples of such distributions can  
 125 be found in Figures 3 and 5. It is vital that this distribution be constructed immediately before the final  
 126  $m_{inv}$  cut, otherwise it would be impossible to estimate the background. As shown in Figures 3 and 5, the  
 127 background is fit (with a polynomial) outside of the peak region of interest to obtain an estimate for the  
 128 background within the region. Within the  $m_{inv}$  cut limits, the background is the region below the fit while  
 129 the signal is the region above the fit.

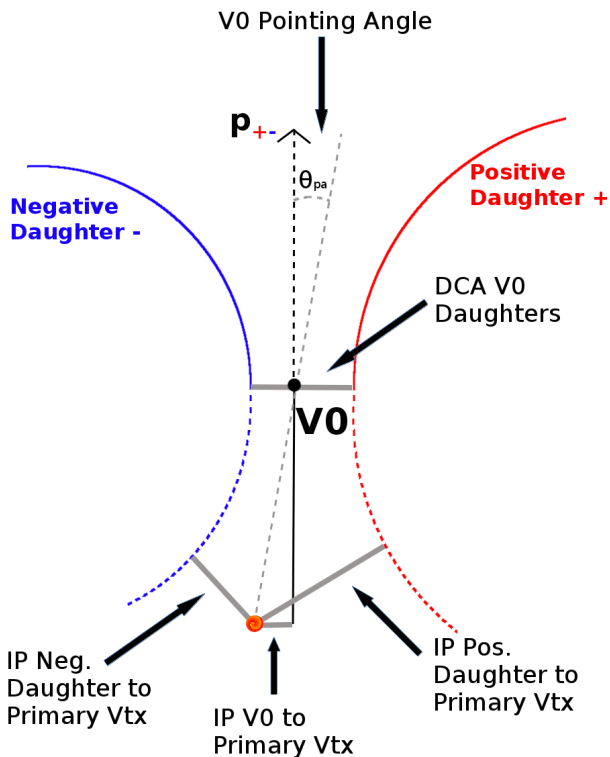


**Fig. 1:** V0 Reconstruction

130 **3.3.1  $\Lambda$  Reconstruction**

131 The following cuts were used to select good  $\Lambda$  ( $\bar{\Lambda}$ ) candidates:

- 132 1. Daughter Particle Cuts

- 133           (a) Cuts Common to Both Daughters
- 134            i.  $|\eta| < 0.8$
- 135            ii. SetTPCnclsDaughters(80)
- 136            iii. SetStatusDaughters(AliESDtrack::kTPCrefic)
- 137            iv. SetMaxDcaV0Daughters(0.4)
- 138           (b) Pion Specific Daughter Cuts
- 139            i.  $p_T > 0.16$
- 140            ii. DCA to prim vertex  $> 0.3$
- 141           (c) Proton Specific Daughter Cuts
- 142            i.  $p_T > 0.5(p) [0.3(\bar{p})] \text{ GeV}/c$
- 143            ii. DCA to prim vertex  $> 0.1$

144        2. V0 Cuts

- 145           (a)  $|\eta| < 0.8$
- 146           (b)  $p_T > 0.4$
- 147           (c)  $|m_{inv} - m_{PDG}| < 3.8 \text{ MeV}$
- 148           (d) DCA to prim. vertex  $< 0.5 \text{ cm}$
- 149           (e) Cosine of pointing angle  $> 0.9993$
- 150           (f) OnFlyStatus = false
- 151           (g) Decay Length  $< 60 \text{ cm}$

152        3. Shared Daughter Cut for V0 Collection

- 153           – Iterate through V0 collection to ensure that no daughter is used in more than one V0 candidate

154       Figure 2a shows the mass assuming  $K_S^0$  hypothesis for the  $\Lambda$  collection, i.e. assume the daughters are  
 155        $\pi^+\pi^-$  instead of  $\pi^+\bar{p}^-$ . Figure 2b is a similar plot, but is for the  $\bar{\Lambda}$  collection, i.e. assume the daughters  
 156       are  $\pi^+\pi^-$  instead of  $\pi^+\bar{p}^-$ . The  $K_S^0$  contamination is visible, although not profound, in both in the slight  
 157       peaks around  $m_{inv} = 0.497 \text{ GeV}/c^2$ . If one simply cuts out the entire peak, good  $\Lambda$  particles will be  
 158       lost. Ideally, the  $\Lambda$  selection and  $K_S^0$  misidentification cuts are selected such that the peak is removed  
 159       from this plot while leaving the distribution continuous. To attempt to remove these  $K_S^0$  contaminations  
 160       without throwing away good  $\Lambda$  and  $\bar{\Lambda}$  particles, the following misidentification cuts are imposed; a  $\Lambda(\bar{\Lambda})$   
 161       candidate is rejected if all of the following criteria are satisfied:

- 162       –  $|m_{inv, K_S^0 \text{ Hypothesis}} - m_{PDG, K_S^0}| < 9.0 \text{ MeV}/c^2$
- 163       – Positive and negative daughters pass  $\pi$  daughter cut implemented for  $K_S^0$  reconstruction
- 164       –  $|m_{inv, K_S^0 \text{ Hypothesis}} - m_{PDG, K_S^0}| < |m_{inv, \Lambda(\bar{\Lambda}) \text{ Hypothesis}} - m_{PDG, \Lambda(\bar{\Lambda})}|$

165       Figure 3 shows the invariant mass ( $M_{inv}$ ) distribution of all  $\Lambda(\bar{\Lambda})$  candidates immediately before the final  
 166       invariant mass cut. These distributions are used to calculate the collection purities. The  $\Lambda$  and  $\bar{\Lambda}$  purities  
 167       are found to be:  $\text{Purity}(\Lambda) \approx \text{Purity}(\bar{\Lambda}) \approx 95\%$ .

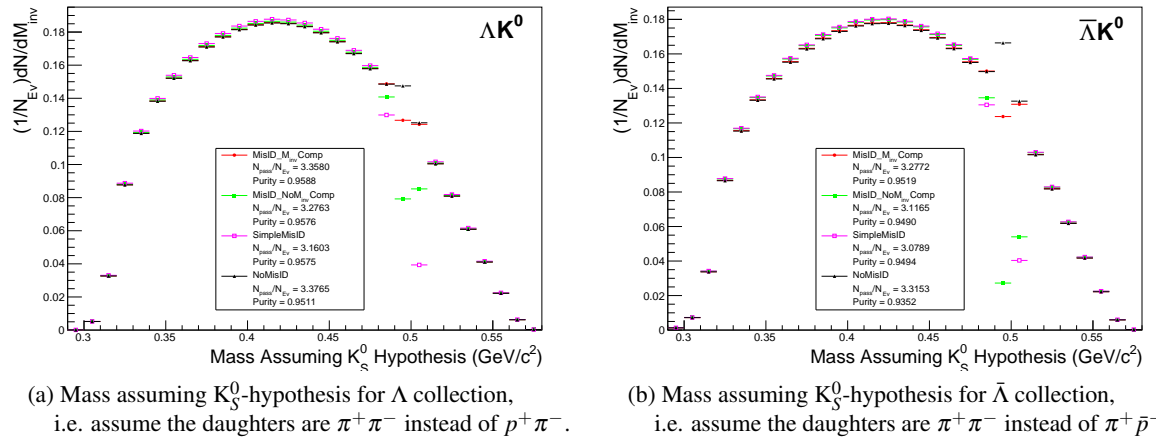


**Fig. 2:** Mass assuming  $K_S^0$ -hypothesis for V0 candidates passing all  $\Lambda$  (2a) and  $\bar{\Lambda}$  (2b) cuts. The “NoMisID” distribution (black triangles) uses the V0 finder without any attempt to remove misidentified  $K_S^0$ . The slight peak in the “NoMisID” distribution around  $m_{inv} = 0.5$  GeV/c<sup>2</sup> contains misidentified  $K_S^0$  particles in our  $\Lambda(\bar{\Lambda})$  collection. “SimpleMisID” (pink squares) simply cuts out the entire peak, which throws away some good  $\Lambda$  and  $\bar{\Lambda}$  particles. “MisID\_NoM<sub>inv</sub>Comp” (green squares) uses the misidentification cut outlined in the text, but does not utilize the invariant mass comparison method. “MisID\_M<sub>inv</sub>Comp” (red circles) utilizes the full misidentification methods, and is currently used for this analysis. “N<sub>pass</sub>/N<sub>ev</sub>” is the total number of  $\Lambda(\bar{\Lambda})$  particles found, normalized by the total number of events. The purity of the collection is also listed.

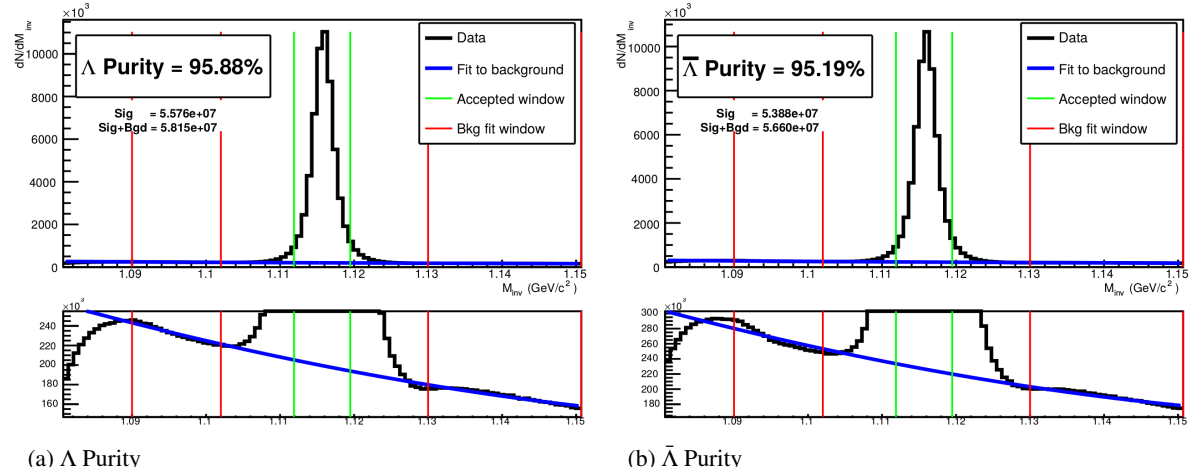


**Fig. 3:** Invariant mass ( $M_{inv}$ ) distribution of all  $\Lambda$  (a) and  $\bar{\Lambda}$  (b) candidates immediately before the final invariant mass cut. The bottom figures are zoomed to show the background with fit. The vertical green lines represent the  $M_{inv}$  cuts used in the analyses, the red vertical lines delineate the region over which the background was fit, and the blue line shows the background fit. These distributions are used to calculate the collection purities, Purity( $\Lambda$ )  $\approx$  Purity( $\bar{\Lambda}$ )  $\approx$  95%.

### 168 3.3.2 $K_S^0$ Reconstruction

169 The following cuts were used to select good  $K_S^0$  candidates:

170 1. Pion Daughter Cuts

- 171 (a)  $|\eta| < 0.8$
- 172 (b) SetTPCnclsDaughters(80)

- 173 (c) SetStatusDaughters(AliESDtrack::kTPCrefic)
- 174 (d) SetMaxDcaV0Daughters(0.3)
- 175 (e)  $p_T > 0.15$
- 176 (f) DCA to prim vertex  $> 0.3$

177 2.  $K_S^0$  Cuts

- 178 (a)  $|\eta| < 0.8$
- 179 (b)  $p_T > 0.2$
- 180 (c)  $m_{PDG} - 13.677 \text{ MeV} < m_{inv} < m_{PDG} + 2.0323 \text{ MeV}$
- 181 (d) DCA to prim. vertex  $< 0.3 \text{ cm}$
- 182 (e) Cosine of pointing angle  $> 0.9993$
- 183 (f) OnFlyStatus = false
- 184 (g) Decay Length  $< 30 \text{ cm}$

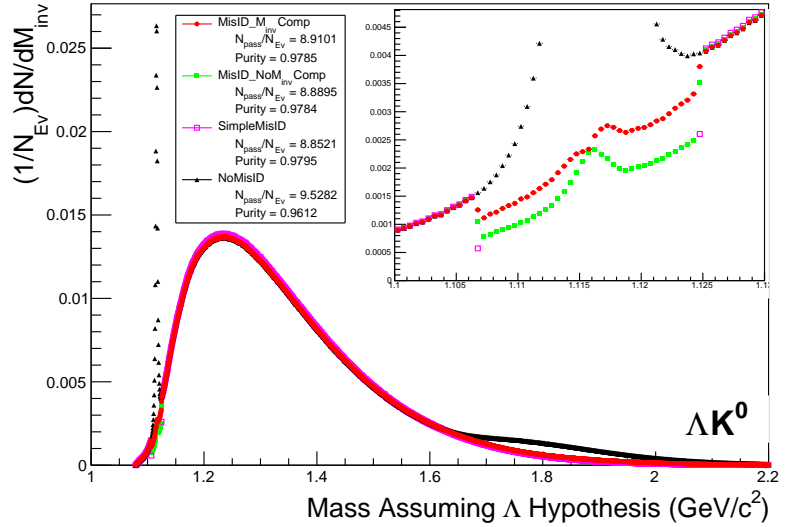
185 3. Shared Daughter Cut for V0 Collection

- 186 – Iterate through V0 collection to ensure that no daughter is used in more than one V0 candidate

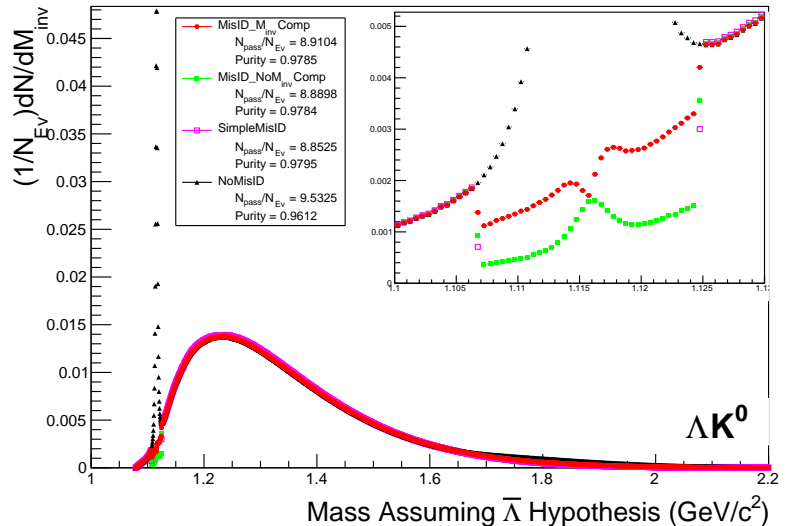
187 As can be seen in Figure 4, some misidentified  $\Lambda$  and  $\bar{\Lambda}$  particles contaminate our  $K_S^0$  sample. Figure  
 188 4a shows the mass assuming  $\Lambda$ -hypothesis for the  $K_S^0$  collection, i.e. assume the daughters are  $p^+\pi^-$   
 189 instead of  $\pi^+\pi^-$ . Figure 4b is similar, but shows the mass assuming  $\bar{\Lambda}$  hypothesis for the collection,  
 190 i.e. assume the daughters are  $\pi^+\bar{p}^-$  instead of  $\pi^+\pi^-$ . The  $\Lambda$  contamination can be seen in 4a, and the  
 191  $\bar{\Lambda}$  contamination in 4b, in the peaks around  $m_{inv} = 1.115 \text{ GeV}/c^2$ . Additionally, the  $\bar{\Lambda}$  contamination is  
 192 visible in Figure 4a, and the  $\Lambda$  contamination visible in Figure 4b, in the region of excess around 1.65  
 193  $< m_{inv} < 2.1 \text{ GeV}/c^2$ . This is confirmed as the number of misidentified  $\Lambda$  particles in the sharp peak  
 194 of Figure 4a (misidentified  $\bar{\Lambda}$  particles in the sharp peak of Figure 4b) approximately equals the excess  
 195 found in the  $1.65 < m_{inv} < 2.1 \text{ GeV}/c^2$  region of Figure 4a (Figure 4b).

196 The peaks around  $m_{inv} = 1.115 \text{ GeV}/c^2$  in Figure 4 contain both misidentified  $\Lambda$  ( $\bar{\Lambda}$ ) particles and good  
 197  $K_S^0$ . If one simply cuts out the entire peak, some good  $K_S^0$  particles will be lost. Ideally, the  $K_S^0$  selection  
 198 and  $\Lambda(\bar{\Lambda})$  misidentification cuts can be selected such that the peak is removed from this plot while leaving  
 199 the distribution continuous. To attempt to remove these  $\Lambda$  and  $\bar{\Lambda}$  contaminations without throwing away  
 200 good  $K_S^0$  particles, the following misidentification cuts are imposed; a  $K_S^0$  candidate is rejected if all of  
 201 the following criteria are satisfied (for either  $\Lambda$  or  $\bar{\Lambda}$  hypothesis):

- 202 –  $|m_{inv, \Lambda(\bar{\Lambda}) \text{ Hypothesis}} - m_{PDG, \Lambda(\bar{\Lambda})}| < 9.0 \text{ MeV}/c^2$
- 203 – Positive daughter passes  $p^+(\pi^+)$  daughter cut implemented for  $\Lambda(\bar{\Lambda})$  reconstruction
- 204 – Negative daughter passes  $\pi^-(\bar{p}^-)$  daughter cut implemented by  $\Lambda(\bar{\Lambda})$  reconstruction
- 205 –  $|m_{inv, \Lambda(\bar{\Lambda}) \text{ Hypothesis}} - m_{PDG, \Lambda(\bar{\Lambda})}| < |m_{inv, K_S^0 \text{ Hypothesis}} - m_{PDG, K_S^0}|$



(a) Mass assuming  $\Lambda$ -hypothesis for  $K_S^0$  collection, i.e. assume the daughters are  $p^+ \pi^-$  instead of  $\pi^+ \pi^-$ .



(b) Mass assuming  $\bar{\Lambda}$ -hypothesis for  $K_S^0$  collection, i.e. assume the daughters are  $\pi^+ \bar{p}^-$  instead of  $\pi^+ \pi^-$ .

**Fig. 4:** Mass assuming  $\Lambda$ -hypothesis (4a) and  $\bar{\Lambda}$ -hypothesis (4b) for  $K_S^0$  collection. The “NoMisID” distribution (black triangles) uses the V0 finder without any attempt to remove misidentified  $\Lambda$  and  $\bar{\Lambda}$ . The peak in the “NoMisID” distribution around  $m_{\text{inv}} = 1.115 \text{ GeV}/c^2$  contains misidentified  $\Lambda$  (4a) and  $\bar{\Lambda}$  (4b) particles in our  $K_S^0$  collection. “SimpleMisID” (pink squares) simply cuts out the entire peak, which throws away some good  $K_S^0$  particles. “MisID\_NoM<sub>inv</sub>Comp” (green squares) uses the misidentification cut outlined in the text, but does not utilize the invariant mass comparison method. “MisID\_M<sub>inv</sub>Comp” (red circles) utilizes the full misidentification methods, and is currently used for this analysis. “ $N_{\text{pass}}/N_{\text{ev}}$ ” is the total number of  $K_S^0$  particles found, normalized by the total number of events. The purity of the collection is also listed. Also note, the relative excess of the “NoMisID” distribution around  $1.65 < m_{\text{inv}} < 2.1 \text{ GeV}/c^2$  shows misidentified  $\bar{\Lambda}$  (4a) and  $\Lambda$  (4b) particles in our  $K_S^0$  collection.

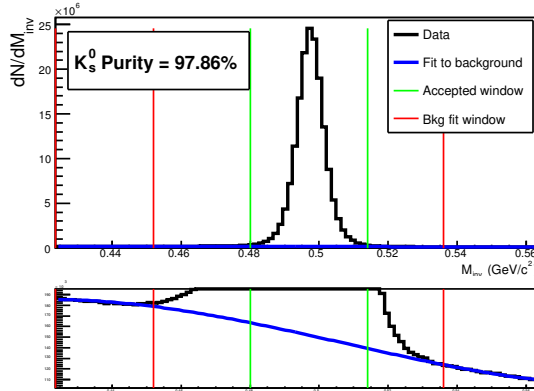


**Fig. 5:** Invariant mass ( $M_{inv}$ ) distribution of all  $K_s^0$  candidates immediately before the final invariant mass cut. The bottom figure is zoomed to show the background with fit. The vertical green lines represent the  $M_{inv}$  cut used in the analyses, the red vertical lines delineate the region over which the background was fit, and the blue line shows the background fit. This distribution is used to calculate the collection purity,  $Purity(K_s^0) \approx 98\%$ .

### 206 3.4 Cascade Reconstruction

207 Our motivation for studying  $\Xi K^\pm$  systems is to hopefully better understand the striking difference in the  
208  $\Lambda K^+$  and  $\Lambda K^-$  data at low  $k^*$  (Figure 14).

209 The reconstruction of  $\Xi$  particles is one step above V0 reconstruction. V0 particles are topologically  
210 reconstructed by searching for the charged daughters' tracks into which they decay. With  $\Xi$  particles, we  
211 search for the V0 particle and charged daughter into which the  $\Xi$  decays. In the case of  $\Xi^-$ , we search  
212 for the  $\Lambda$  (V0) and  $\pi^-$  (track) daughters. We will refer to this  $\pi$  as the “bachelor  $\pi$ ”.

213 The following cuts were used to select good  $\Xi^-$  ( $\bar{\Xi}^+$ ) candidates:

214 1. V0 Daughter Reconstruction

215 (a) V0 Daughter Particle Cuts

216 i. Cuts Common to Both Daughters

- 217 A.  $|\eta| < 0.8$
- 218 B. SetTPCnclsDaughters(80)
- 219 C. SetStatusDaughters(AliESDtrack::kTPCrefic)
- 220 D. SetMaxDcaV0Daughters(0.4)

221 ii. Pion Specific Daughter Cuts

- 222 A.  $p_T > 0.16$
- 223 B. DCA to prim vertex  $> 0.3$
- 224 iii. Proton Specific Daughter Cuts
- 225 A.  $p_T > 0.5(p) [0.3(\bar{p})]$  GeV/ $c$
- 226 B. DCA to prim vertex  $> 0.1$

227 (b) V0 Cuts

- 228 i.  $|\eta| < 0.8$
- 229 ii.  $p_T > 0.4$  GeV/ $c$
- 230 iii.  $|m_{inv} - m_{PDG}| < 3.8$  MeV
- 231 iv. DCA to prim. vertex  $> 0.2$  cm
- 232 v. Cosine of pointing angle to  $\Xi$  decay vertex  $> 0.9993$

233                 vi. OnFlyStatus = false  
 234                 vii. Decay Length < 60 cm  
 235                 viii. The misidentification cuts described in Section 3.3.1 are utilized  
 236     2. Bachelor  $\pi$  Cuts  
 237         (a)  $|\eta| < 0.8$   
 238         (b)  $p_T < 100 \text{ GeV}/c$   
 239         (c) DCA to prim vertex > 0.1 cm  
 240         (d) SetTPCnclsDaughters(70)  
 241         (e) SetStatusDaughters(AliESDtrack::kTPCrefic)  
 242     3.  $\Xi$  Cuts  
 243         (a)  $|\eta| < 0.8$   
 244         (b)  $0.8 < p_T < 100 \text{ GeV}/c$   
 245         (c)  $|m_{inv} - m_{PDG}| < 3.0 \text{ MeV}$   
 246         (d) DCA to prim. vertex < 0.3 cm  
 247         (e) Cosine of pointing angle > 0.9992  
 248     4. Shared Daughter Cut for  $\Xi$  Collection  
 249         – Iterate through  $\Xi$  collection to ensure that no daughter is used in more than one  $\Xi$  candidate

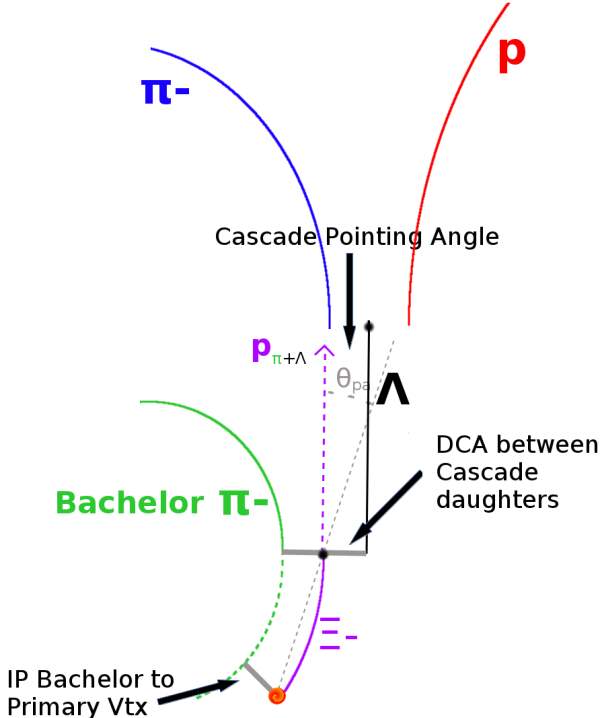


**Fig. 6:**  $\Xi$  Reconstruction

250     The purity of our  $\Xi$  and  $\bar{\Xi}$  collections are calculated just as those of our V0 collections 3.3. Figure 7,  
 251     which is used to calculate the purity, shows the  $m_{inv}$  distribution of our  $\Xi(\bar{\Xi})$  candidates just before the  
 252     final  $m_{inv}$  cut. Currently, we have Purity( $\Xi^-$ )  $\approx 90\%$  and Purity( $\bar{\Xi}^+$ )  $\approx 92\%$ .

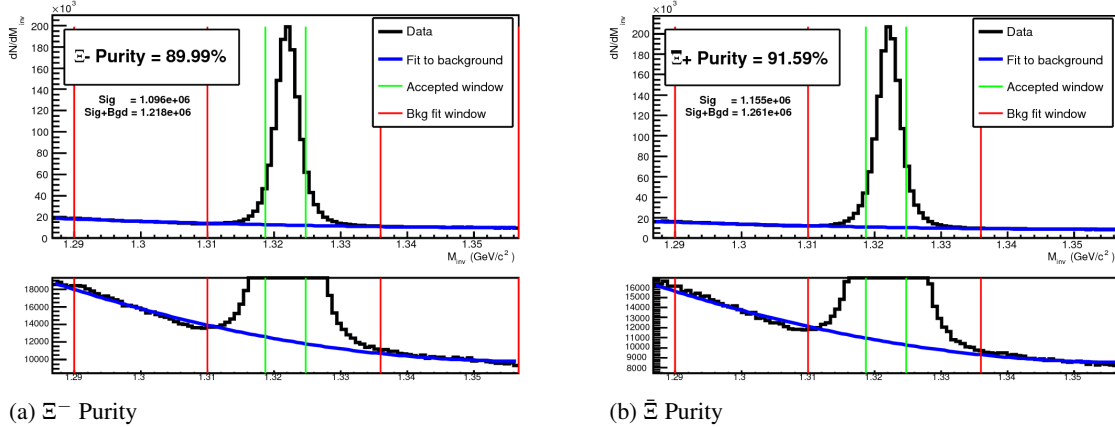


**Fig. 7:**  $\Xi^-$  ( $\bar{\Xi}^+$ ) Purity 0-10%: Purity( $\Xi^-$ )  $\approx$  90% and Purity( $\bar{\Xi}^+$ )  $\approx$  92%.

### 253 3.5 Pair Selection

254 It is important to obtain true particle pairs in the analysis. In particular, contamination from pairs con-  
 255 structed with split or merged tracks, and pairs sharing daughters, can introduce an artificial signal into  
 256 the correlation function, obscuring the actual physics.

257 1. Shared Daughter Cut for Pairs

258 (a) V0-V0 Pairs (i.e.  $\Lambda(\bar{\Lambda})K_S^0$  analyses)

- 259 – Remove all pairs which share a daughter
- 260 – Ex.  $\Lambda$  and  $K_S^0$  particles which share a  $\pi^-$  daughter are not included

261 (b) V0-Track Pairs (i.e.  $\Lambda(\bar{\Lambda})K^\pm$  analyses)

- 262 – Remove pairs if Track is also used as a daughter of the V0
- 263 – In these analyses, this could only occur if, for instance, a  $K$  is misidentified as a  $\pi$
- 264 – or  $p$  in the V0 reconstruction

265 (c)  $\Xi$ -Track Pairs

- 266 – Remove pairs if Track is also used as a daughter of the  $\Xi$
- 267 – In these analyses, this could only occur if, for instance, a  $K$  is misidentified as a  $\pi$
- 268 – or  $p$  in the V0 reconstruction, or misidentified as bachelor  $\pi$ .
- 269 – Remove pair if bachelor  $\pi$  is also a daughter of the  $\Lambda$
- 270 – This is not a pair cut, but is included here because this cut occurs in the
- 271 – AliFemtoXiTrackPairCut class

272 2. Average Separation Cuts

- 273 – Used to cut out splitting and merging effects
- 274 – The motivation for these cuts can be seen in Figures 8, 9, and 10, in which average separation
- 275 – correlation functions are presented

276 (a)  $\Lambda(\bar{\Lambda})K_S^0$  Analyses

- 277 – Average separation  $> 6.0$  cm for like charge sign daughters
- 278 – ex.  $p$  daughter of  $\Lambda$  and  $\pi^+$  daughter of  $K_S^0$
- 279 – No cut for unlike-sign daughters

280 (b)  $\Lambda(\bar{\Lambda})K^\pm$  Analyses

- 281 – Average Separation > 8.0 cm for daughter of  $\Lambda(\bar{\Lambda})$  sharing charge sign of  $K^\pm$   
 282 – ex. in  $\Lambda K^+$  analysis,  $p$  daughter of  $\Lambda$  with  $K^+$   
 283 – No cut for unlike signs

284 (c)  $\Xi(\bar{\Xi})K^\pm$  Analyses

- 285 – Average Separation > 8.0 cm for any daughter of  $\Xi$  sharing charge sign of  $K^\pm$   
 286 – ex. in  $\Xi^- K^-$  analysis,  $\pi^-$  daughter of  $\Lambda$  daughter with  $K^-$ , and bachelor  $\pi^-$  daugh-  
 287 ter with  $K^-$   
 288 – No cut for unlike signs

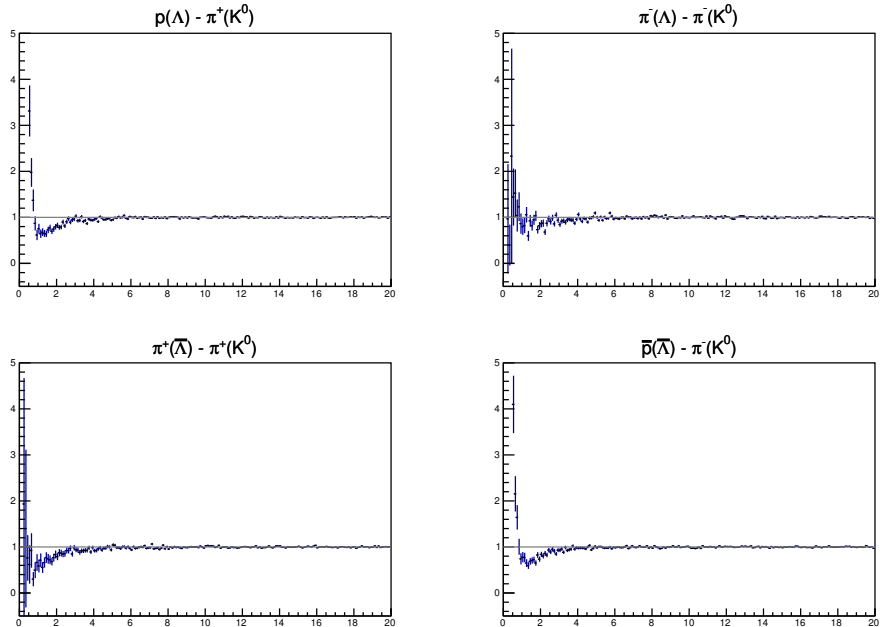


**Fig. 8:** Average separation (cm) correlation functions of  $\Lambda(\bar{\Lambda})$  and  $K_S^0$  Daughters. Only like-sign daughter pairs are shown (the distributions for unlike-signs were found to be flat). The title of each subfigure shows the daughter pair, as well as the mother of each daughter (in “()”), ex. top left is  $p$  from  $\Lambda$  with  $\pi^+$  from  $K_S^0$ .

289 **4 Correlation Functions**

290 This analysis studies the momentum correlations of both  $\Lambda$ -K and  $\Xi$ -K pairs using the two-particle cor-  
 291 relation function, defined as  $C(k^*) = A(k^*)/B(k^*)$ , where  $A(k^*)$  is the signal distribution,  $B(k^*)$  is the  
 292 reference (or background) distribution, and  $k^*$  is the momentum of one of the particles in the pair rest  
 293 frame. In practice,  $A(k^*)$  is constructed by binning in  $k^*$  pairs from the same event. Ideally,  $B(k^*)$  is sim-  
 294 ilar to  $A(k^*)$  in all respects excluding the presence of femtoscopic correlations [2]; as such,  $B(k^*)$  is used  
 295 to divide out the phase-space effects, leaving only the femtoscopic effects in the correlation function.

296 In practice,  $B(k^*)$  is obtained by forming mixed-event pairs, i.e. particles from a given event are paired  
 297 with particles from  $N_{mix}(= 5)$  other events, and these pairs are then binned in  $k^*$ . In forming the back-  
 298 ground distribution, it is important to mix only similar events; mixing events with different phase-spaces  
 299 can lead to artificial signals in the correlation function. Therefore, in this analysis, we mix events with  
 300 primary vertices within 2 cm and centralities within 5% of each other. Also note, a vertex correction is  
 301 also applied to each event, which essentially re-centers the primary vertices to  $z = 0$ .

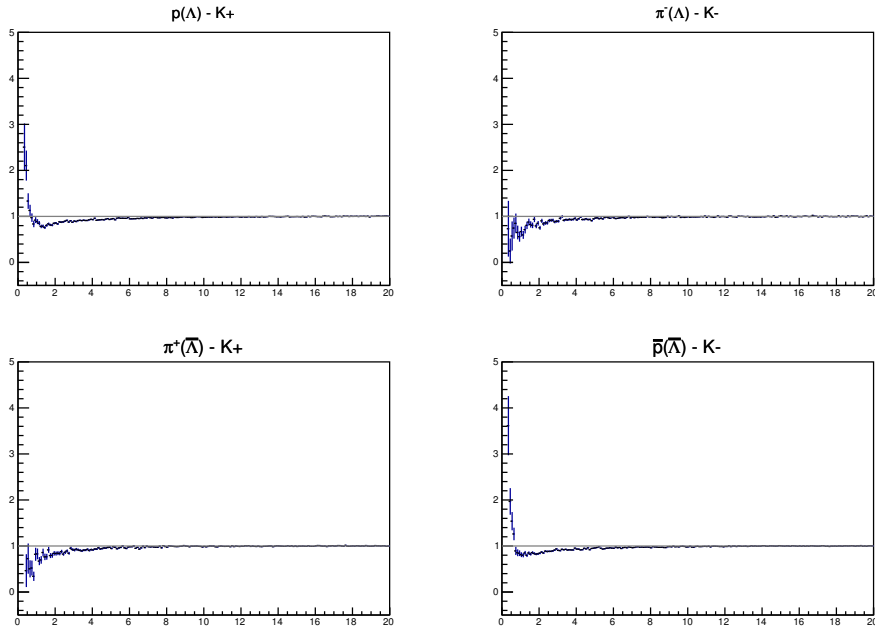


**Fig. 9:** Average separation (cm) correlation functions of  $\Lambda(\bar{\Lambda})$  Daughter and  $K^\pm$ . Only like-sign pairs are shown (unlike-signs were flat). In the subfigure titles, the particles in “()” represent the mothers, ex. top left is  $p$  from  $\Lambda$  with  $K^+$ .

302 This analysis presents correlation functions for three centrality bins (0-10%, 10-30%, and 30-50%),  
 303 and is currently pair transverse momentum ( $k_T = 0.5|\mathbf{p}_{T,1} + \mathbf{p}_{T,2}|$ ) integrated (i.e. not binned in  $k_T$ ).  
 304 The correlation functions are constructed separately for the two magnetic field configurations, and are  
 305 combined using a weighted average:

$$C_{combined}(k^*) = \frac{\sum_i w_i C_i(k^*)}{\sum_i w_i} \quad (3)$$

306 where the sum runs over the correlation functions to be combined, and the weight,  $w_i$ , is the number of  
 307 numerator pairs in  $C_i(k^*)$ . Here, the sum is over the two field configurations.

308 Figures 11, 12, and 13 show the correlation functions for all centralities studied for  $\Lambda K_S^0(\bar{\Lambda} K_S^0)$ ,  $\Lambda K^+(\bar{\Lambda} K^-)$ ,  
 309 and  $\Lambda K^-(\bar{\Lambda} K^+)$ , respectively. All were normalized in the range  $0.32 < k^* < 0.4$  GeV/c.

## 310 5 Fitting

### 311 5.1 Model: $\Lambda K_S^0$ , $\Lambda K^\pm$ , $\Xi^{ch} K_S^0$

312 The two-particle relative momentum correlation function may be written theoretically by the Koonin-  
 313 Pratt equation [3, 4]:

$$C(\mathbf{k}^*) = \int S(\mathbf{r}^*) |\Psi_{\mathbf{k}^*}(\mathbf{r}^*)|^2 d^3 \mathbf{r}^* \quad (4)$$

314 In the absence of Coulomb effects, and assuming a spherically gaussian source of width  $R$ , the 1D  
 315 femtoscopic correlation function can be calculated analytically using:

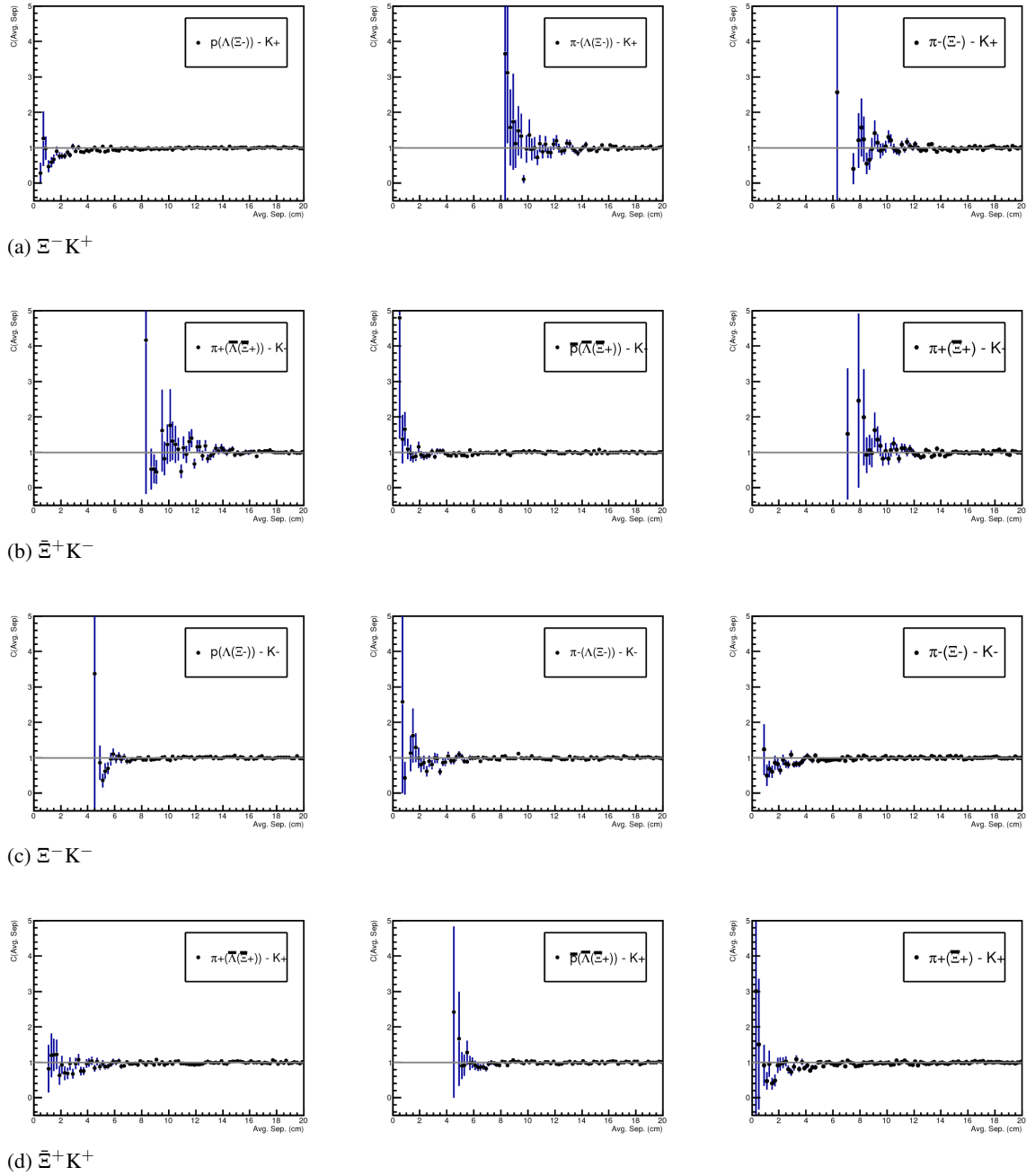


**Fig. 10:** Average separation (cm) correlation functions of  $\Xi$  Daughter and  $K^\pm$ . In the subfigure titles, the particles in “( )” represent the mothers, ex. top left is  $p$  from  $\Lambda$  from  $\Xi^-$  with  $K^+$ .

$$C(k^*) = 1 + \lambda [C_{QI}(k^*) + C_{FSI}(k^*)] \quad (5)$$

<sup>316</sup>  $C_{QI}$  describes plane-wave quantum interference:

$$C_{QI}(k^*) = \alpha \exp(-4k^{*2}R^2) \quad (6)$$

<sup>317</sup> where  $\alpha = (-1)^{2j}/(2j+1)$  for identical particles with spin  $j$ , and  $\alpha = 0$  for non-identical particles.  
<sup>318</sup> Obviously,  $\alpha = 0$  for all analyses presented in this note.  $C_{FSI}$  describes the s-wave strong final state  
<sup>319</sup> interaction between the particles:

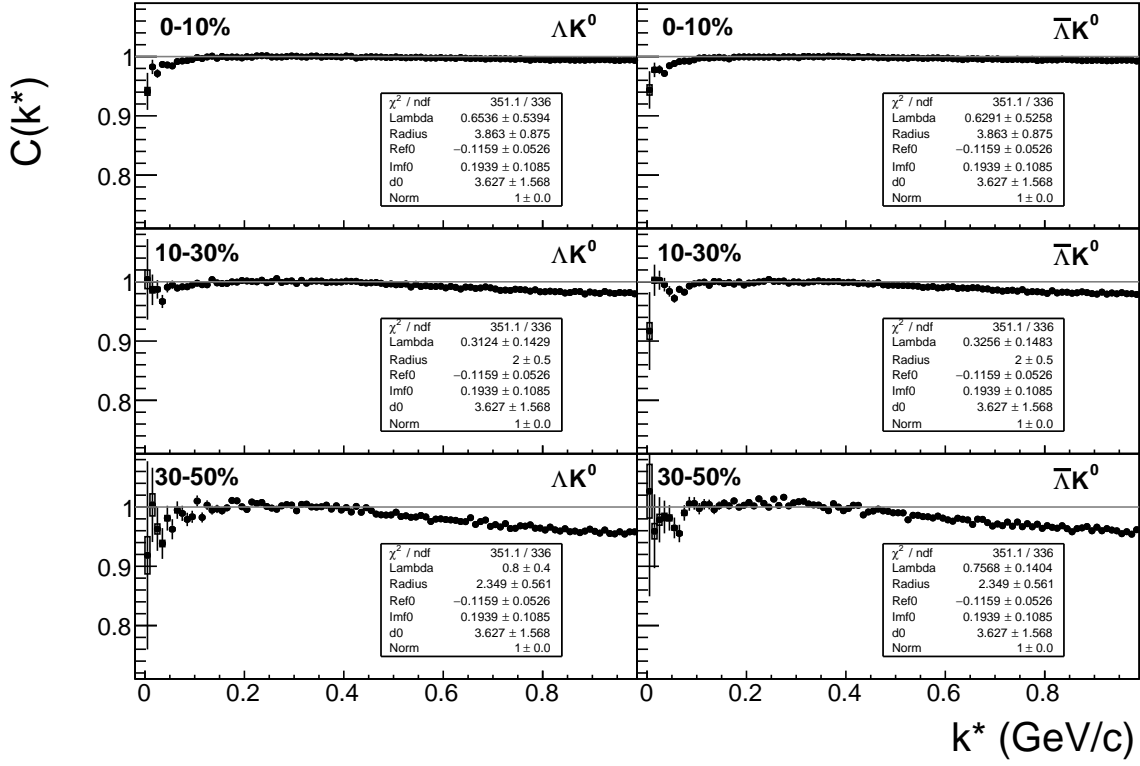


**Fig. 11:**  $\Lambda K_S^0$  (left) and  $\bar{\Lambda} K_S^0$  (right) correlation functions for 0-10% (top), 10-30% (middle), and 30-50% (bottom) centralities. The lines represent the statistical errors, while the boxes represent the systematic errors.

$$C_{FSI}(k^*) = (1 + \alpha) \left[ \frac{1}{2} \left| \frac{f(k^*)}{R} \right|^2 \left( 1 - \frac{d_0}{2\sqrt{\pi}R} \right) + \frac{2\Re f(k^*)}{\sqrt{\pi}R} F_1(2k^*R) - \frac{\Im f(k^*)}{R} F_2(2k^*R) \right] \quad (7)$$

$$f(k^*) = \left( \frac{1}{f_0} + \frac{1}{2} d_0 k^{*2} - ik^* \right)^{-1}; \quad F_1(z) = \int_0^z \frac{e^{x^2-z^2}}{x} dx; \quad F_2(z) = \frac{1-e^{-z^2}}{z}$$

where  $R$  is the source size,  $f(k^*)$  is the s-wave scattering amplitude,  $f_0$  is the complex scattering length, and  $d_0$  is the effective range of the interaction.

The code developed to fit the data is called “LednickyFitter”, and utilizes the ROOT TMinuit implementation of the MINUIT fitting package. In short, given a function with a number of parameters, the fitter explores the parameter space searching for the minimum of the equation. In this implementation, the function to be minimized should represent the difference between the measure and theoretical correlation functions. However, a simple  $\chi^2$  test is inappropriate for fitting correlation functions, as the ratio two Poisson distributions does not result in a Poisson distribution. Instead, a log-likelihood fit function of the following form is used [2]:

$$\chi_{PML}^2 = -2 \left[ A \ln \left( \frac{C(A+B)}{A(C+1)} \right) + B \ln \left( \frac{A+B}{B(C+1)} \right) \right] \quad (8)$$

where  $A$  is the experimental signal distribution (numerator),  $B$  is the experimental background distribution (denominator), and  $C$  is the theoretical fit correlation function.

The LednickyFitter uses Equations 5 – 7 to build the theoretical fit, and Equation 8 as the statistic quantifying the quality of the fit. The parameters to be varied by MINUIT are:  $\lambda$ ,  $R$ ,  $f_0$  ( $\Re f_0$  and  $\Im f_0$  separately),  $d_0$ , and normalization  $N$ . The fitter currently includes methods to correct for momentum resolution and

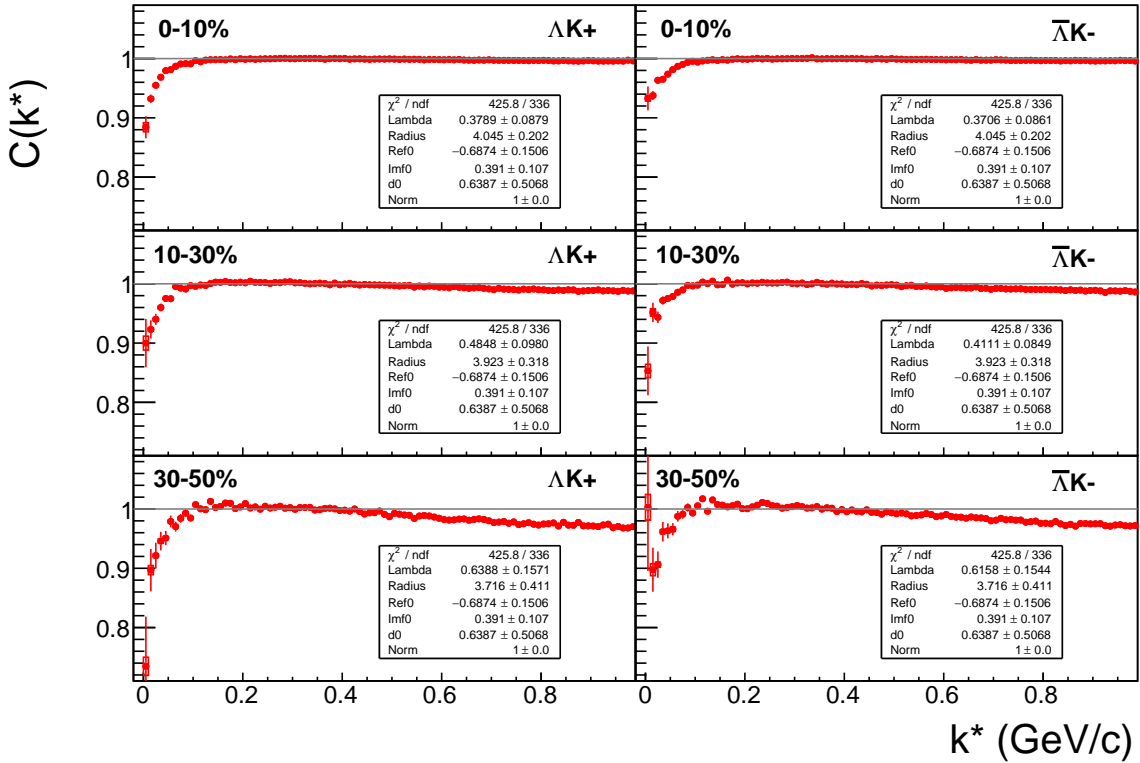


**Fig. 12:**  $\Lambda K^+$  (left) and  $\bar{\Lambda} K^-$  (right) correlation functions for 0-10% (top), 10-30% (middle), and 30-50% (bottom) centralities. The lines represent the statistical errors, while the boxes represent the systematic errors.

a non-flat background. These corrections are applied to the fit function, the data is never touched. The fitter is able to share parameters between different analyses and fit all simultaneously.

In a typical fit, a given pair is fit with its conjugate (ex.  $\Lambda K^+$  with  $\bar{\Lambda} K^-$ ) across all centralities (0-10%, 10-30%, 30-50%), for a total of 6 simultaneous analyses. Each analysis has a unique  $\lambda$  and normalization parameter. The radii are shared between analyses of like centrality, as these should have similar source sizes. The scattering parameters ( $R_{f0}, I_{f0}, d_0$ ) are shared amongst all.

Figures 19, 21, and 23 (Section 7) show experimental data with fits for all studied centralities for  $\Lambda K_S^0$  with  $\bar{\Lambda} K_S^0$ ,  $\Lambda K^+$  with  $\bar{\Lambda} K^-$ , and  $\Lambda K^-$  with  $\bar{\Lambda} K^+$ , respectively. In the figures, the black solid line represents the “raw” fit, i.e. not corrected for momentum resolution effects nor non-flat background. The green line shows the fit to the non-flat background. The purple points show the fit after momentum resolution and non-flat background corrections have been applied. The initial values of the parameters is listed, as well as the final fit values with uncertainties.

## 5.2 Model: $\Xi^{ch} K^{ch}$

When fitting the  $\Xi^-(\bar{\Xi}^+)K^\pm$  results, it is necessary to include both strong and Coulomb effects. In this case, Equation 5 is no longer valid, and, in fact, there is no analytical form with which to fit. Therefore, we must begin with the wave function describing the pair interaction, and simulate many particle pairs to obtain a theoretical fit correlation function. The code developed to achieve this functionality is called “CoulombFitter”. Currently, in order to generate the statistics needed for a stable fit, we find that  $\sim 10^4$  simulated pairs per 10 MeV bin are necessary. Unfortunately, the nature of this process means that the “CoulombFitter” takes much longer to run than the “LednickýFitter” of Section 5.1.

The two-particle correlation function may be written as:

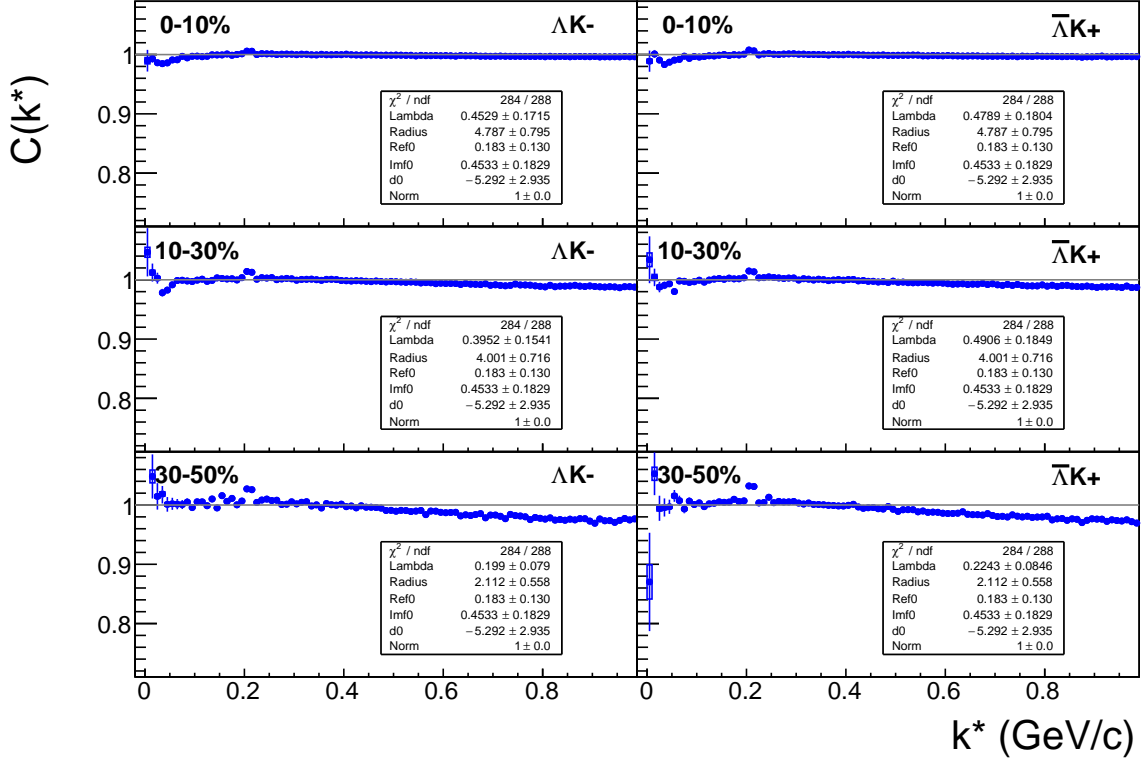


**Fig. 13:**  $\Lambda K^-$  (left) and  $\bar{\Lambda} K^+$  (right) correlation functions for 0-10% (top), 10-30% (middle), and 30-50% (bottom) centralities. The lines represent the statistical errors, while the boxes represent the systematic errors. The peak at  $k^* \approx 0.2$  GeV/c is due to the  $\Omega^-$  resonance.

$$C(\mathbf{k}^*) = \sum_S \rho_S \int S(\mathbf{r}^*) |\Psi_{\mathbf{k}^*}^S(\mathbf{r}^*)|^2 d^3 \mathbf{r}^* \quad (9)$$

where  $\rho_S$  is the normalized emission probability of particles in a state with spin  $S$ ,  $S(\mathbf{r}^*)$  is the pair emission source distribution (assumed to be Gaussian), and  $\Psi_{\mathbf{k}^*}^S(\mathbf{r}^*)$  is the two-particle wave-function including both strong and Coulomb interactions [5]:

$$\Psi_{\mathbf{k}^*}(\mathbf{r}^*) = e^{i\delta_c} \sqrt{A_c(\eta)} [e^{i\mathbf{k}^* \cdot \mathbf{r}^*} F(-i\eta, 1, i\xi) + f_c(k^*) \frac{\tilde{G}(\rho, \eta)}{r^*}] \quad (10)$$

where  $\rho = k^* r^*$ ,  $\eta = (k^* a_c)^{-1}$ ,  $\xi = \mathbf{k}^* \cdot \mathbf{r}^* + k^* r^* \equiv \rho(1 + \cos \theta^*)$ , and  $a_c = (\mu z_1 z_2 e^2)^{-1}$  is the two-particle Bohr radius (including the sign of the interaction).  $\delta_c$  is the Coulomb s-wave phase shift,  $A_c(\eta)$  is the Coulomb penetration factor,  $\tilde{G} = \sqrt{A_c}(G_0 + iF_0)$  is a combination of the regular ( $F_0$ ) and singular ( $G_0$ ) s-wave Coulomb functions.  $f_c(k^*)$  is the s-wave scattering amplitude:

$$f_c(k^*) = [\frac{1}{f_0} + \frac{1}{2} d_0 k^{*2} - \frac{2}{a_c} h(\eta) - ik^* A_c(\eta)]^{-1} \quad (11)$$

where, the “h-function”,  $h(\eta)$ , is expressed through the digamma function,  $\psi(z) = \Gamma'(z)/\Gamma(z)$  as:

$$h(\eta) = 0.5[\psi(i\eta) + \psi(-i\eta) - \ln(\eta^2)] \quad (12)$$

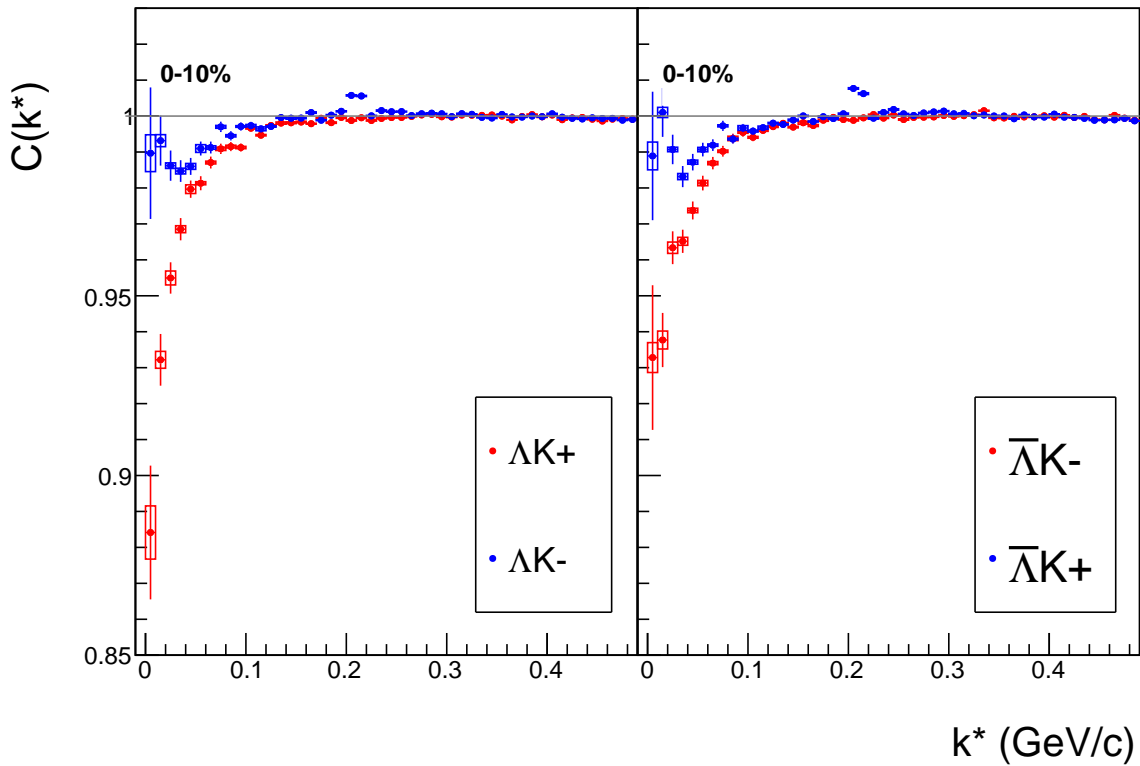


**Fig. 14:** Correlation Functions:  $\Lambda K^+$  vs  $\Lambda K^-$  ( $\bar{\Lambda} K^+$  vs  $\bar{\Lambda} K^-$ ) for 0-10% centrality. The peak in  $\Lambda K^-$  ( $\bar{\Lambda} K^+$ ) at  $k^* \approx 0.2 \text{ GeV}/c$  is due to the  $\Omega^-$  resonance. The lines represent the statistical errors. (NOTE: This figure is slightly dated, and a new one will be generated which includes both statistical and systematic uncertainties)

363 Unfortunately, with this analysis, we are not sensitive to, and therefore not able to distinguish between,  
364 the iso-spin singlet and triplet states. We proceed with our analysis, but the results must be interpreted  
365 as iso-spin averaged scattering parameters.

366 As stated before, to generate a fit correlation function, we must simulate a large number of pairs, calculate  
367 the wave-function, and average  $\Psi^2$  over all pairs in a given  $k^*$  bin. Essentially, we calculate Equation 9  
368 by hand:

$$\begin{aligned} C(\mathbf{k}^*) &= \sum_S \rho_S \int S(\mathbf{r}^*) |\Psi_{\mathbf{k}^*}^S(\mathbf{r}^*)|^2 d^3 \mathbf{r}^* \\ &\longrightarrow C(|\mathbf{k}^*|) \equiv C(k^*) = \sum_S \rho_S \langle |\Psi^S(\mathbf{k}_i^*, \mathbf{r}_i^*)|^2 \rangle_i \\ &\longrightarrow C(k^*) = \lambda \sum_S \rho_S \langle |\Psi^S(\mathbf{k}_i^*, \mathbf{r}_i^*)|^2 \rangle_i + (1 - \lambda) \end{aligned} \quad (13)$$

369 where  $\langle \rangle_i$  represents an average over all pairs in a given  $k^*$  bin.

370 In summary, for a given  $k^*$  bin, we must draw  $N_{\text{pairs}} \sim 10^4$  pairs, and for each pair:

- 371 1. Draw a random  $\mathbf{r}^*$  vector according to our Gaussian source distribution  $S(\mathbf{r}^*)$   
372 2. Draw a random  $\mathbf{k}^*$  vector satisfying the  $|\mathbf{k}^*|$  restriction of the bin  
373 – We draw from real  $k^*$  vectors obtained from the data

374 – However, we find that drawing from a distribution flat in  $k^*$  gives similar results

375 3. Construct the wave-function  $\Psi$

376 After all pairs for a given  $k^*$  bin are simulated and wave-functions obtained, the results are averaged to  
377 give the fit result.

378 Construction of the wave-functions, Equation 10, involves a number of complex functions not included  
379 in standard C++ or ROOT libraries (namely,  $h(\eta)$ ,  $\tilde{G}(\rho, \eta)$ ), and  $F(-i\eta, 1, i\xi)$ . These functions were  
380 even difficult to find and implement from elsewhere. Our solution was to embed a Mathematica kernel  
381 into our C++ code to evaluate these functions. However, having Mathematica work on-the-fly with the  
382 fitter was far too time consuming (fitter would have taken day, maybe weeks to finish). Our solution  
383 was to use Mathematica to create matrices representing these functions for different parameter values.  
384 During fitting, these matrices were then interpolated and the results used to build the wave-functions.  
385 This method decreased the running time dramatically, and we are not able to generate results in under  $\sim$   
386 1 hour. This process will be explained in more detail in future versions of the note.

387 **5.3 Momentum Resolution Corrections**

388 Finite track momentum resolution causes the reconstructed momentum of a particle to smear around the  
389 true value. This, of course, also holds true for V0 particles. The effect is propagated up to the pairs  
390 of interest, which causes the reconstructed relative momentum ( $k_{Rec}^*$ ) to differ from the true momentum  
391 ( $k_{True}^*$ ). Smearing of the momentum typically will result in a suppression of the signal.

392 The effect of finite momentum resolution can be investigated using the MC data, for which both the true  
393 and reconstructed momenta are available. Figure 15 shows sample  $k_{True}^*$  vs.  $k_{Rec}^*$  plots for  $\Lambda(\bar{\Lambda})K^\pm$  0-  
394 10% analyses; Figure 15a was generated using same-event pairs, while Figure 15b was generated using  
395 mixed-event pairs (with  $N_{mix} = 5$ ).

396 If there are no contaminations in our particle collection, the plots in Figure 15 should be smeared around  
397  $k_{True}^* = k_{Rec}^*$ ; this is mostly true in our analyses. However, there are some interesting features of our results  
398 which demonstrate a small (notice the log-scale on the z-axis) contamination in our particle collection.  
399 The structure around  $k_{Rec}^* = k_{True}^* - 0.15$  is mainly caused by  $K_S^0$  contamination in our  $\Lambda(\bar{\Lambda})$  sample. The  
400 remaining structure not distributed about  $k_{Rec}^* = k_{True}^*$  is due to  $\pi$  and  $e$  contamination in our  $K^\pm$  sample.  
401 These contaminations are more visible in Figure 16, which show  $k_{Rec}^*$  vs.  $k_{True}^*$  plots (for a small sample  
402 of the  $\Lambda K^\pm$  0-10% central analysis), for which the MC truth (i.e. true, known identity of the particle)  
403 was used to eliminate misidentified particles in the  $K^+(a)$  and  $\Lambda(b)$  collections. (NOTE: This is an old  
404 figure and is for a small sample of the data. A new version will be generated shortly. It, nonetheless,  
405 demonstrates the point well).

406 Information gained from looking at  $k_{Rec}^*$  vs  $k_{True}^*$  can be used to apply corrections to account for the  
407 effects of finite momentum resolution on the correlation functions. A typical method involves using the  
408 MC HIJING data to build two correlation functions,  $C_{Rec}(k^*)$  and  $C_{True}(k^*)$ , using the generator-level  
409 momentum ( $k_{True}^*$ ) and the measured detector-level momentum ( $k_{Rec}^*$ ). The data is then corrected by  
410 multiplying by the ratio,  $C_{True}/C_{Rec}$ , before fitting. This essentially unsmears the data, which that can  
411 be compared directly to theoretical predictions and fits. Although this is conceptually simple, there are  
412 a couple of big disadvantages to this method. First, HIJING does not incorporate final-state interactions,  
413 so weights must be used when building same-event (numerator) distributions. These weights account for  
414 the interactions, and, in the absence of Coulomb interactions, can be calculated using Eq. 5. Of course,  
415 these weights are valid only for a particular set of fit parameters. Therefore, in the fitting process, during  
416 which the fitter explores a large parameter set, the corrections will not remain valid. As such, applying  
417 the momentum resolution correction and fitting becomes a long and drawn out iterative process. An initial  
418 parameter set is obtained (through fitting without momentum resolution corrections, theoretical models,

419 or a good guess), then the MC data is run over to obtain the correction factor, the data is fit using the  
 420 correction factor, a refined parameter set is extracted, the MC data is run over again to obtain the new  
 421 correction factor, etc. This process continues until the parameter set stabilizes. The second issue concerns  
 422 statistics. With the MC data available on the grid, we were not able to generate the statistics necessary  
 423 to use the raw  $C_{True}/C_{Rec}$  ratio. The ratio was not stable, and when applied to the data, obscured the  
 424 signal. Attempting to fit the ratio to use to generate the corrections also proved problematic. However, as  
 425 HIJING does not include final-state interactions, the same-event and mixed-event pairs are very similar  
 426 (with the exception of things like energy and momentum conservation, etc). Therefore, one may build  
 427 the numerator distribution using mixed-event pairs. This corresponds, more or less, to simply running a  
 428 the weight generator through the detector framework.

429 A second approach is to use information gained from plots like those in Figure 15, which can be consid-  
 430 ered response matrices. The response matrix describes quantitatively how each  $k_{Rec}^*$  bin receives contribu-  
 431 tions from multiple  $k_{True}^*$  bins, and can be used to account for the effects of finite momentum resolution.  
 432 With this approach, the resolution correction is applied on-the-fly during the fitting process by propagat-  
 433 ing the theoretical (fit) correlation function through the response matrix, according to:

$$C_{fit}(k_{Rec}^*) = \frac{\sum_{k_{True}^*} M_{k_{Rec}^*, k_{True}^*} C_{fit}(k_{True}^*)}{\sum_{k_{True}^*} M_{k_{Rec}^*, k_{True}^*}} \quad (14)$$

434 where  $M_{k_{Rec}^*, k_{True}^*}$  is the response matrix (Figure 15),  $C_{fit}(k_{True}^*)$  is the fit binned in  $k_{True}^*$ , and the denomi-  
 435 nator normalizes the result.

436 Equation 14 describes that, for a given  $k_{Rec}^*$  bin, the observed value of  $C(k_{Rec}^*)$  is a weighted average of  
 437 all  $C(k_{True}^*)$  values, where the weights are the normalized number of counts in the  $[k_{Rec}^*, k_{True}^*]$  bin. As  
 438 seen in Figure 15, overwhelmingly the main contributions comes from the  $k_{Rec}^* = k_{True}^*$  bins. Although  
 439 the correction is small, it is non-negligible for the low- $k^*$  region of the correlation function.

440 Here, the momentum resolution correction is applied to the fit, not the data. In other words, during  
 441 fitting, the theoretical correlation function is smeared just as real data would be, instead of unsmeared  
 442 the data. This may not be ideal for the theorist attempting to compare a model to experimental data, but  
 443 it leaves the experimental data unadulterated. The current analyses use this second approach to applying  
 444 momentum resolution corrections because of two major advantages. First, the MC data must be analyzed  
 445 only once, and no assumptions about the fit are needed. Secondly, the momentum resolution correction  
 446 is applied on-the-fly by the fitter, delegating the iterative process to a computer instead of the user.

#### 447 5.4 Residual Correlations

448 The purpose of this analysis is study the interaction and scale of the emitting source of the pairs. In order  
 449 to obtain correct results, it is important for our particle collections to consist of primary particles. In  
 450 practice, this is difficult to achieve for our  $\Lambda$  and  $\bar{\Lambda}$  collections. Many of our  $\Lambda$  particles are not primary,  
 451 but originate as decay products from other hyperons, including  $\Sigma^0$ ,  $\Xi^-$ ,  $\Xi^0$  and  $\Omega^-$ . In these decays,  
 452 the  $\Lambda$  carries away a momentum very similar to that of its parent. As a result, the correlation function  
 453 between a secondary  $\Lambda$  and, for instance, a  $K^+$  will be sensitive to, and dependent upon, the interaction  
 454 between the parent of the  $\Lambda$  and the  $K^+$ . In effect, the correlation between the parent of the  $\Lambda$  and the  $K^+$   
 455 (ex.  $\Sigma^0 K^+$ ) will be visible, although smeared out, in the  $\Lambda K^+$  data. We call this a residual correlation  
 456 resulting from feed-down.

457 As it is difficult for us to eliminate these residual correlations in our analyses, we must attempt to account  
 458 for them in our fitter. To achieve this, we will simultaneously fit the data for both the primary correlation  
 459 function and the residual correlations. For example, in the simple case of a  $\Lambda K^+$  analysis with residuals

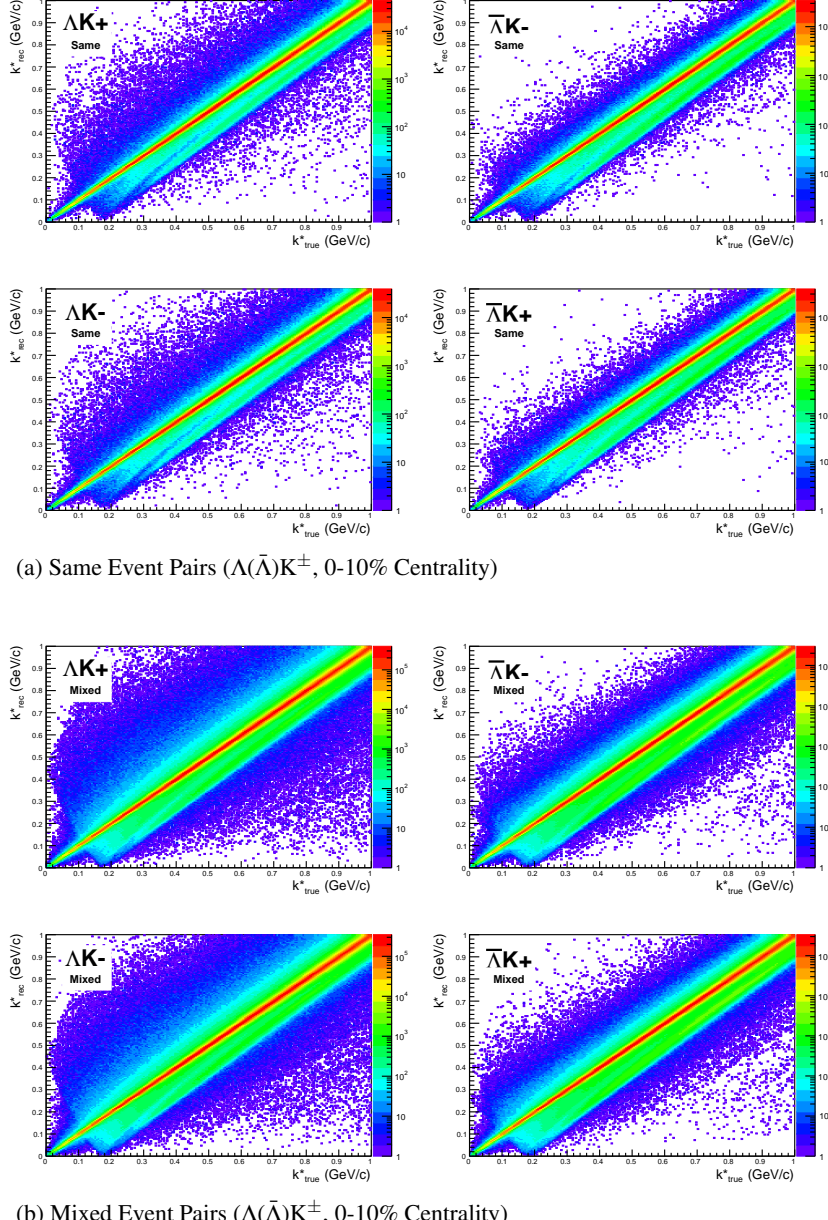


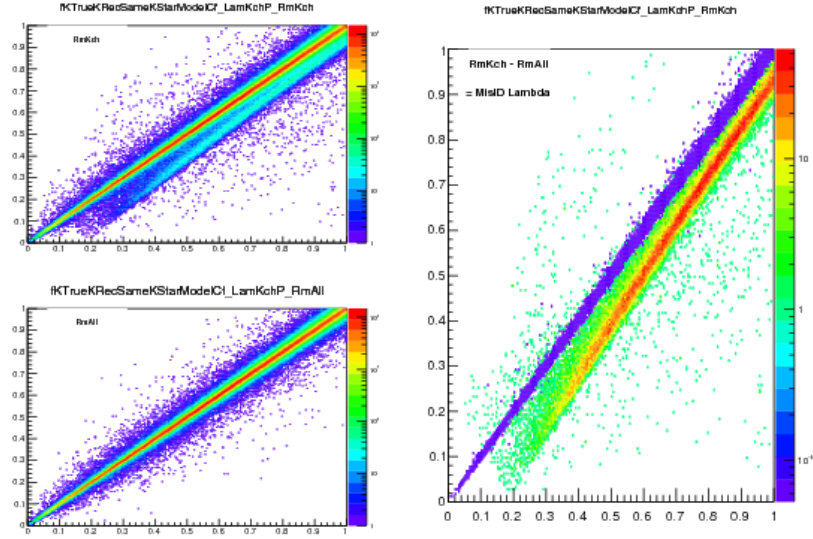
**Fig. 15:** Sample  $k_{True}^*$  vs.  $k_{Rec}^*$  plot for  $\Lambda(\bar{\Lambda})K^\pm$  0-10% analyses. The structure which appears around  $k_{Rec}^* = k_{True}^* - 0.15$  is mainly caused by  $K_S^0$  contamination in our  $\Lambda(\bar{\Lambda})$  sample. The remaining structure not distributed about  $k_{Rec}^* = k_{True}^*$  is due to  $\pi$  and  $e$  contamination in our  $K^\pm$  sample. These contaminations are more clearly visible in Figure 16

arising solely from  $\Sigma^0 K^+$  feed-down:

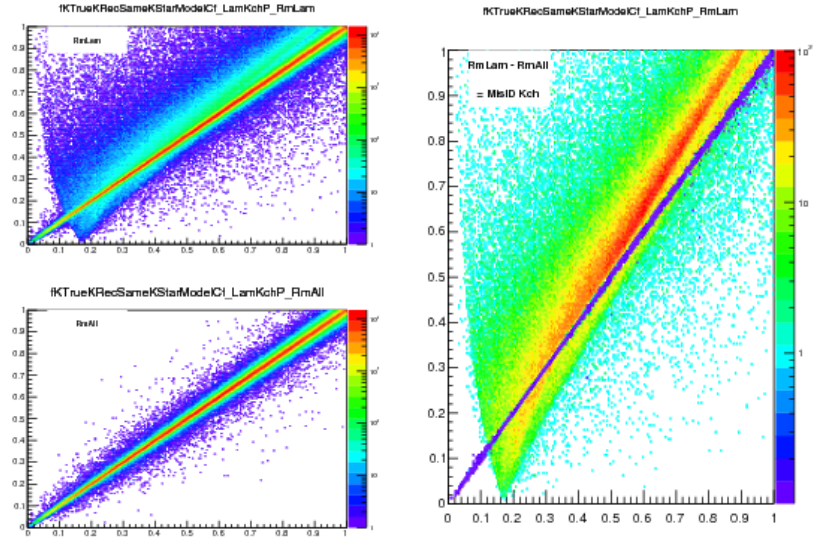
$$C_{measured}(k_{\Lambda K^+}^*) = 1 + \lambda_{\Lambda K^+}[C_{\Lambda K^+}(k_{\Lambda K^+}^*) - 1] + \lambda_{\Sigma^0 K^+}[C_{\Sigma^0 K^+}(k_{\Lambda K^+}^*) - 1]$$

$$C_{\Sigma^0 K^+}(k_{\Lambda K^+}^*) \equiv \sum_{k_{\Sigma^0 K^+}^*} \frac{C_{\Sigma^0 K^+}(k_{\Sigma^0 K^+}^*) T(k_{\Sigma^0 K^+}^*, k_{\Lambda K^+}^*)}{T(k_{\Sigma^0 K^+}^*, k_{\Lambda K^+}^*)} \quad (15)$$

$C_{\Sigma^0 K^+}(k_{\Sigma^0 K^+}^*)$  is the  $\Sigma^0 K^+$  correlation function from, for instance, Equation 5, and  $T$  is the transform matrix generated with THERMINATOR. This equation can be easily extended to include feed-down



(a) (Top Left) All misidentified  $K^+$  excluded. (Bottom Left) All misidentified  $\Lambda$  and  $K^+$  excluded. (Right) The difference of (Top Left) - (Bottom Left), which reveals the contamination in our  $\Lambda$  collection. The structure which appears around  $k_{Rec}^* = k_{True}^* - 0.15$  is mainly caused by  $K_S^0$  contamination in our  $\Lambda(\bar{\Lambda})$  sample.



(b) (Top Left) All misidentified  $\Lambda$  excluded. (Bottom Left) All misidentified  $\Lambda$  and  $K^+$  excluded. (Right) The difference of (Top Left) - (Bottom Left), which reveals the contamination in our  $K^+$  collection. The structure not distributed about  $k_{Rec}^* = k_{True}^*$  is due to  $\pi$  and  $e^-$  contamination in our  $K^\pm$  sample.

**Fig. 16:** Note: This is an old figure and is for a small sample of the data. A new version will be generated shortly.  
 $y\text{-axis} = k_{Rec}^*$ ,  $x\text{-axis} = k_{True}^*$ .

(Left)  $k_{Rec}^*$  vs.  $k_{True}^*$  plots for a small sample of the  $\Lambda K^+$  0-10% central analysis, MC truth was used to eliminate misidentified particles in the  $K^+$ (a) and  $\Lambda$ (b) collections. (Right) The difference of the top left and bottom left plots. Contaminations in our particle collections are clearly visible. Figure (a) demonstrates a  $K_S^0$  contamination in our  $\Lambda$  collection; Figure (b) demonstrates a  $\pi$  and  $e^-$  contamination in our  $K^\pm$  collection.

$$C_{measured}(k_{\Lambda K}^*) = \sum_i \lambda_i C_i(k_{\Lambda K}^*) \quad (16)$$

464 The framework for extracting the necessary transform matrices from the THERMINATOR data is already  
 465 in place, and has been used to generate the examples from  $\Lambda K^+$  and  $\bar{\Lambda} K^+$  analyses shown in Figures 17  
 466 and 18. However, these residual correlations have not yet been implemented in the fitter.

467 There is an obvious added complication here, as, for instance, the  $\Xi^- K^\pm$  residuals necessitate the in-  
 468 clusion of the CoulombFitter into the process. The complication of combining the two fitters is not as  
 469 troubling as the increase in fitting time that this is sure to bring. Additionally, in the future, we may  
 470 combine our  $\Lambda K$  and  $\Xi K$  analyses to be fit simultaneously.

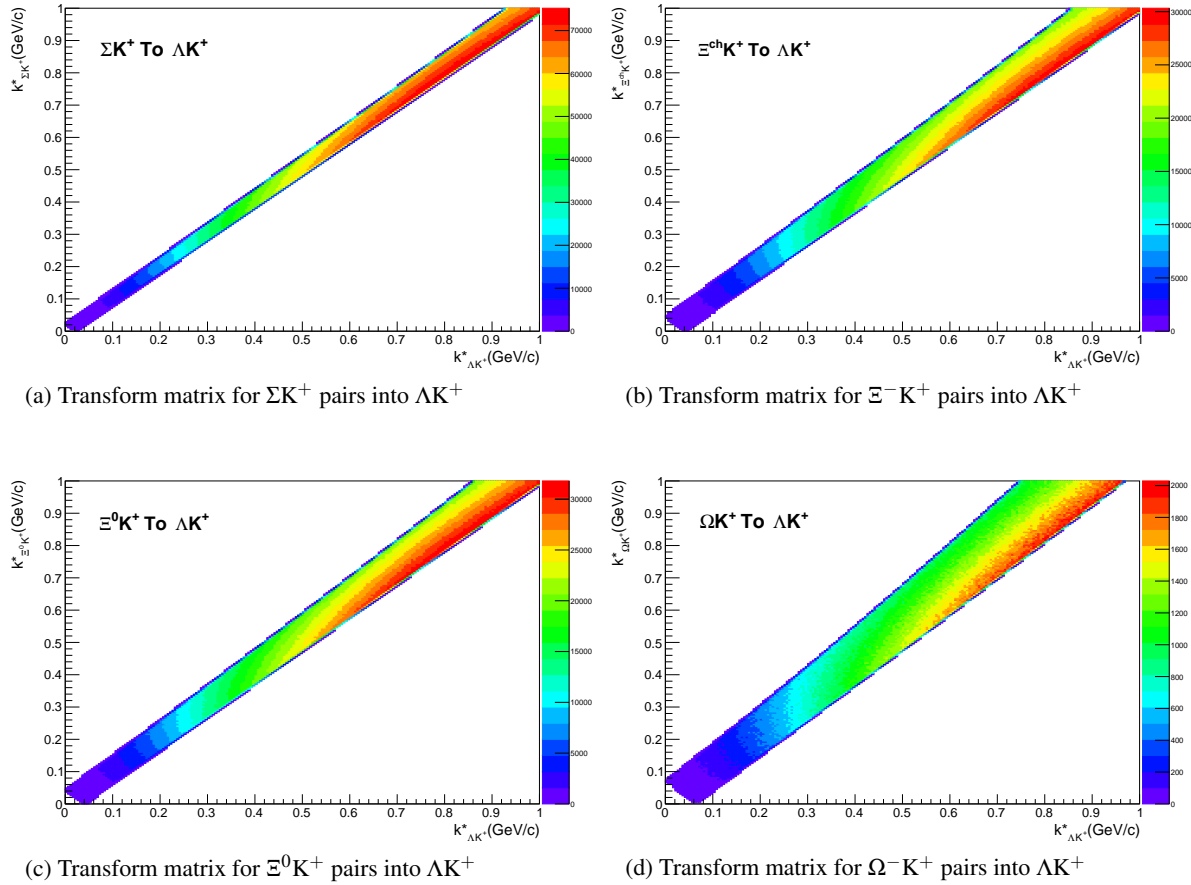


**Fig. 17:** Transform Matrices generated with THERMINATOR for  $\Lambda K^+$  Analysis

## 471 6 Systematic Errors

472 In order to understand my systematic uncertainties, the analysis code was run many times using slightly  
 473 different values for a number of important cuts, and the results were compared.

474 In order to quantify the systematic errors on the data, all correlation functions built using all varied cut  
 475 values were bin-by-bin averaged, and the resulting variance of each bin was taken as the systematic error.  
 476 The cuts which were utilized in this study are presented in Sections 6.1.1 ( $\Lambda K_S^0$ ) and 6.2.1 ( $\Lambda K^\pm$ ).

477 Similarly, the fit parameters extracted from all of these correlation functions were averaged, and the  
 478 resulting variances were taken as the systematic errors for the fit parameters. As with the systematic

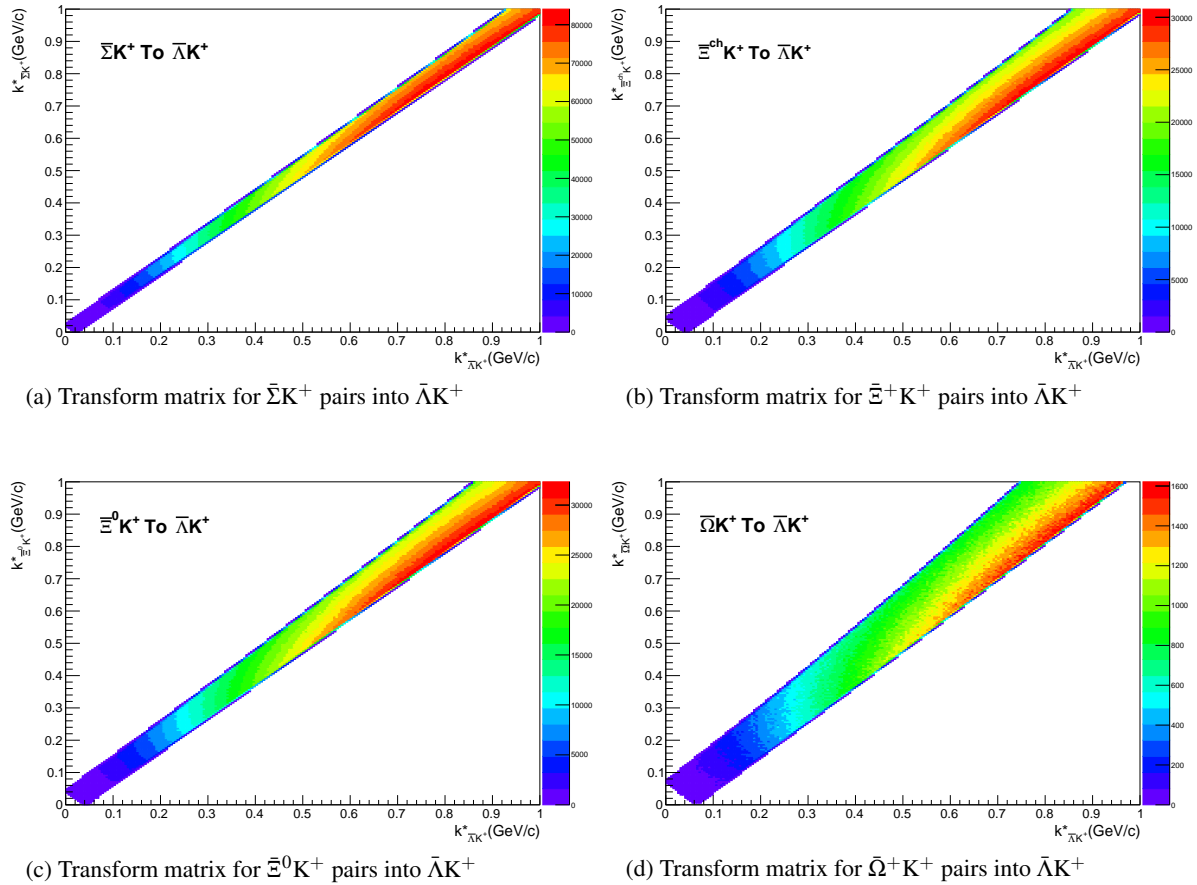


**Fig. 18:** Transform Matrices generated with THERMINATOR for  $\bar{\Lambda}K^+$  Analysis

479 errors on the data, this was performed for all varied cut values. Additionally, a systematic analysis was  
 480 done on our fit method (which, for now, just includes our choice of fit range). These two sources of  
 481 uncertainty were combined in quadrature to obtain the final systematic uncertainties on the extracted fit  
 482 parameters.

## 483 6.1 Systematic Errors: $\Lambda K_S^0$

### 484 6.1.1 Particle and Pair Cuts

485 The cuts included in the systematic study, as well as the values used in the variations, are listed below.  
 486 Note, the central value corresponds to that used in the analysis.

- 487 1. DCA  $\Lambda(\bar{\Lambda})$ : {4, 5, 6 mm}
- 488 2. DCA  $K_S^0$ : {2, 3, 4 mm}
- 489 3. DCA  $\Lambda(\bar{\Lambda})$  Daughters: {3, 4, 5 mm}
- 490 4. DCA  $K_S^0$  Daughters: {2, 3, 4 mm}
- 491 5.  $\Lambda(\bar{\Lambda})$  Cosine of Pointing Angle: {0.9992, 0.9993, 0.9994}
- 492 6.  $K_S^0$  Cosine of Pointing Angle: {0.9992, 0.9993, 0.9994}
- 493 7. DCA to Primary Vertex of  $p(\bar{p})$  Daughter of  $\Lambda(\bar{\Lambda})$ : {0.5, 1, 2 mm}

- 494     8. DCA to Primary Vertex of  $\pi^-(\pi^+)$  Daughter of  $\Lambda(\bar{\Lambda})$ : {2, 3, 4 mm}
- 495     9. DCA to Primary Vertex of  $\pi^+$  Daughter of  $K_S^0$ : {2, 3, 4 mm}
- 496    10. DCA to Primary Vertex of  $\pi^-$  Daughter of  $K_S^0$ : {2, 3, 4 mm}
- 497   11. Average Separation of Like-Charge Daughters: {5, 6, 7 cm}

498   **6.1.2 Non-Flat Background**

499   We fit our non-flat background with a linear function. To study the contribution of this choice to our sys-  
500   tematic errors, we also fit with a quadratic and Gaussian form. The resulting uncertainties are combined  
501   with the uncertainties arising from our particle cuts.

502   **6.1.3 Fit Range**

503   Our choice of  $k^*$  fit range was varied by  $\pm 25\%$ . The resulting uncertainties in the extracted parameter  
504   sets were combined with our uncertainties arising from our particle and pair cuts.

505   **6.2 Systematic Errors:  $\Lambda K^\pm$**

506   **6.2.1 Particle and Pair Cuts**

507   The cuts included in the systematic study, as well as the values used in the variations, are listed below.  
508   Note, the central value corresponds to that used in the analysis.

- 509   1. DCA  $\Lambda(\bar{\Lambda})$ : {4, 5, 6 mm}
- 510   2. DCA  $\Lambda(\bar{\Lambda})$  Daughters: {3, 4, 5 mm}
- 511   3.  $\Lambda(\bar{\Lambda})$  Cosine of Pointing Angle: {0.9992, 0.9993, 0.9994}
- 512   4. DCA to Primary Vertex of  $p(\bar{p})$  Daughter of  $\Lambda(\bar{\Lambda})$ : {0.5, 1, 2 mm}
- 513   5. DCA to Primary Vertex of  $\pi^-(\pi^+)$  Daughter of  $\Lambda(\bar{\Lambda})$ : {2, 3, 4 mm}
- 514   6. Average Separation of  $\Lambda(\bar{\Lambda})$  Daughter with Same Charge as  $K^\pm$ : {7, 8, 9 cm}
- 515   7. Max. DCA to Primary Vertex in Transverse Plane of  $K^\pm$ : {1.92, 2.4, 2.88}
- 516   8. Max. DCA to Primary Vertex in Longitudinal Direction of  $K^\pm$ : {2.4, 3.0, 3.6}

517   **6.2.2 Non-Flat Background**

518   We fit our non-flat background with a linear function. To study the contribution of this choice to our sys-  
519   tematic errors, we also fit with a quadratic and Gaussian form. The resulting uncertainties are combined  
520   with the uncertainties arising from our particle cuts.

521   **6.2.3 Fit Range**

522   Our choice of  $k^*$  fit range was varied by  $\pm 25\%$ . The resulting uncertainties in the extracted parameter  
523   sets were combined with our uncertainties arising from our particle and pair cuts.

524 **6.3 Systematic Errors:  $\Xi K^\pm$**

525 **6.3.1 Particle and Pair Cuts**

526 The cuts included in the systematic study, as well as the values used in the variations, are listed below.  
527 Note, the central value corresponds to that used in the analysis.

- 528 1. Max. DCA  $\Xi(\bar{\Xi})$ : {x, y, z mm}
- 529 2. Max. DCA  $\Xi(\bar{\Xi})$  Daughters: {x, y, z mm}
- 530 3. Min.  $\Xi(\bar{\Xi})$  Cosine of Pointing Angle to Primary Vertex: {0.9991, 0.9992, 0.9993}
- 531 4. Min.  $\Lambda(\bar{\Lambda})$  Cosine of Pointing Angle to  $\Xi(\bar{\Xi})$  Decay Vertex: {0.9992, 0.9993, 0.9994}
- 532 5. Min. DCA Bachelor  $\pi$ : {0.2, 0.3, 0.4 mm}
- 533 6. Min. DCA  $\Lambda(\bar{\Lambda})$ : {0.5, 1, 2 mm}
- 534 7. Max. DCA  $\Lambda(\bar{\Lambda})$  Daughters: {3, 4, 5 mm}
- 535 8. Min.  $\Lambda(\bar{\Lambda})$  Cosine of Pointing Angle To Primary Vertex: {0.9992, 0.9993, 0.9994}
- 536 9. Min. DCA to Primary Vertex of  $p(\bar{p})$  Daughter of  $\Lambda(\bar{\Lambda})$ : {0.5, 1, 2 mm}
- 537 10. Min. DCA to Primary Vertex of  $\pi^-(\pi^+)$  Daughter of  $\Lambda(\bar{\Lambda})$ : {2, 3, 4 mm}
- 538 11. Min. Average Separation of  $\Lambda(\bar{\Lambda})$  Daughter and  $K^\pm$  with like charge: {7, 8, 9 cm}
- 539 12. Min. Average Separation of Bachelor  $\pi$  and  $K^\pm$  with like charge: {x, y, z cm}
- 540 13. Max. DCA to Primary Vertex in Transverse Plane of  $K^\pm$ : {1.92, 2.4, 2.88}
- 541 14. Max. DCA to Primary Vertex in Longitudinal Direction of  $K^\pm$ : {2.4, 3.0, 3.6}

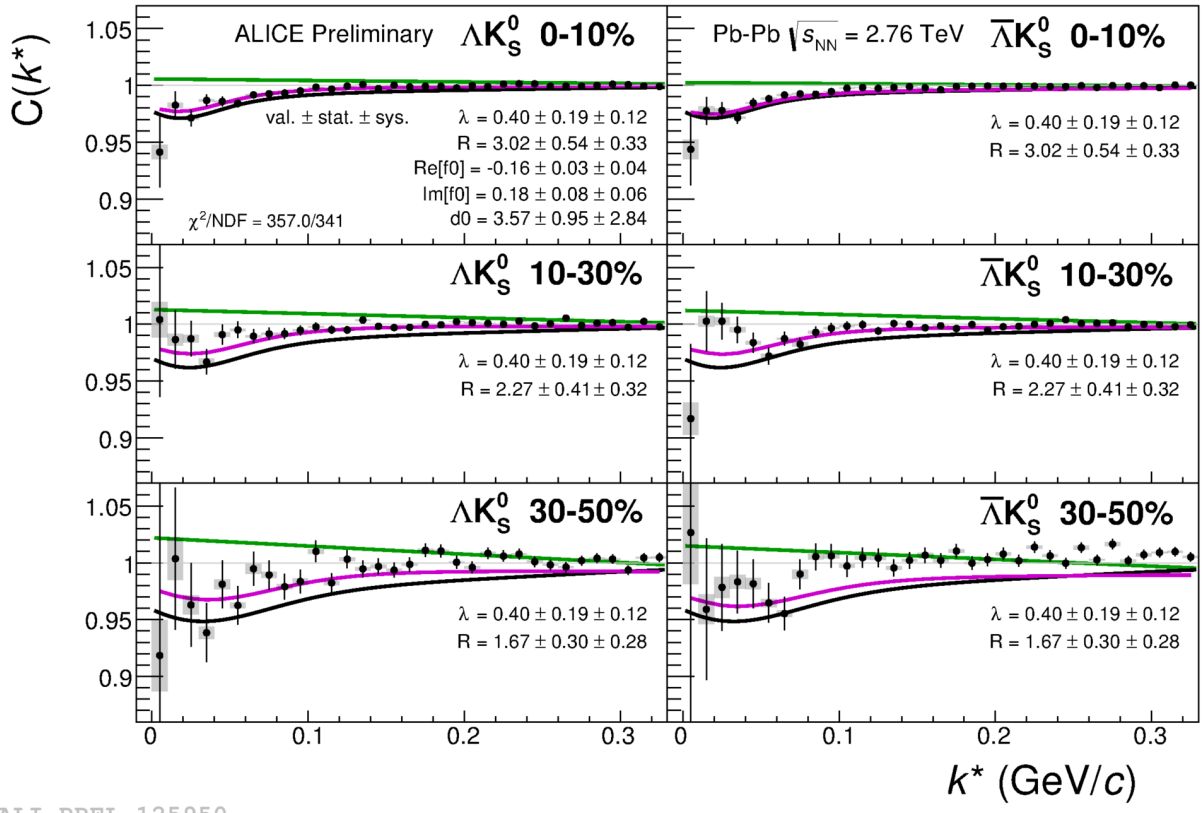
542 **7 Results and Discussion**

543 **7.1 Results:  $\Lambda K_S^0$  and  $\Lambda K^\pm$**

544 Figures 19, 21, and 23 (Section 7) show experimental data with fits for all studied centralities for  $\Lambda K_S^0$   
545 with  $\bar{\Lambda} K_S^0$ ,  $\Lambda K^+$  with  $\bar{\Lambda} K^-$ , and  $\Lambda K^-$  with  $\bar{\Lambda} K^+$ , respectively. The parameter sets extracted from the fits  
546 can be found in Tables 1 and 2. All correlation functions were normalized in the range  $0.32 < k^* < 0.40$   
547 GeV/c, and fit in the range  $0.0 < k^* < 0.30$  GeV/c. For the  $\Lambda K^-$  and  $\bar{\Lambda} K^+$  analyses, the region  $0.19 < k^* < 0.23$  GeV/c was excluded from the fit to exclude the bump caused by the  $\Omega^-$  resonance. The  
549 non-flat background was fit with a linear form from  $0.6 < k^* < 0.9$  GeV/c. The theoretical fit function  
550 was then multiplied by this background during the fitting process.

551 In the figures (19, 21, and 23), the black solid line represents the “raw” fit, i.e. not corrected for momen-  
552 tum resolution effects nor non-flat background. The green line shows the fit to the non-flat background.  
553 The purple points show the fit after momentum resolution and non-flat background corrections have been  
554 applied. The initial values of the parameters is listed, as well as the final fit values with uncertainties.

555 For the  $\Lambda K_S^0$  fits,  $R$  was restricted to [2.0, 10.0 fm] and  $\Lambda$  was restricted to [0.1, 0.8]. This gave the lowest  
556  $\chi^2$  value, but loosening this restriction changes the fit parameters slightly. Notice, the 10-30% radius is  
557 at its limit, as is  $\lambda$  from the 30-50%  $\Lambda K_S^0$  analysis. This accounts for the 0.000 systematic uncertainty of  
558 the 10-30%  $R$  value currently quoted in Table 1. An estimate for this uncertainty should be included in  
559 the next version of this note. In the future, we may need to throw out the 30-50% data from the fit, but  
560 this is not ideal.



ALI-PREL-125950

**Fig. 19:** Fits to the  $\Lambda K_S^0$  (left) and  $\bar{\Lambda} K_S^0$  (right) data for the centralities 0-10% (top), 10-30% (middle), and 30-50% (bottom). The lines represent the statistical errors, while the boxes represent the systematic errors. Each has unique  $\lambda$  and normalization parameters. The radii are shared amongst like centralities; the scattering parameters ( $\text{Re}[f_0]$ ,  $\text{Im}[f_0]$ ,  $d_0$ ) are shared amongst all. The black solid line represents the “raw” fit, i.e. not corrected for momentum resolution effects nor non-flat background. The green line shows the fit to the non-flat background. The purple points show the fit after momentum resolution and non-flat background corrections have been applied. The initial values of the parameters is listed, as well as the final fit values with uncertainties. Here,  $R$  was restricted to [2.,10.] and  $\Lambda$  was restricted to [0.1,0.8].

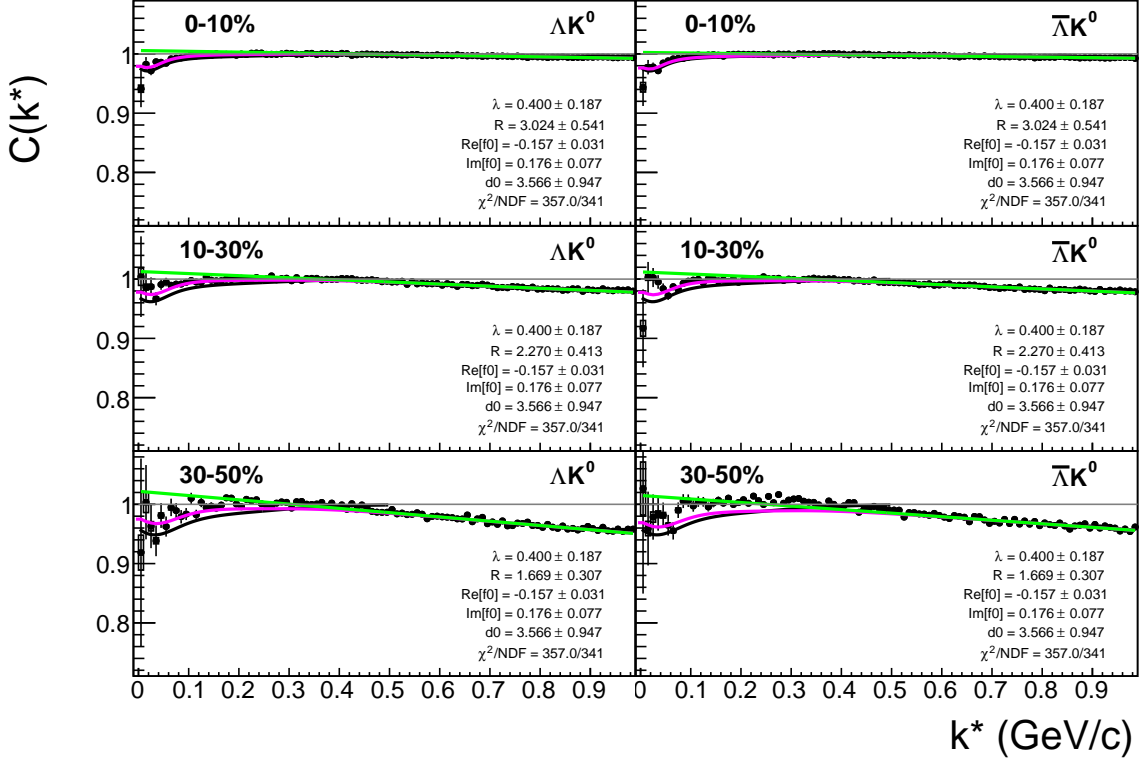
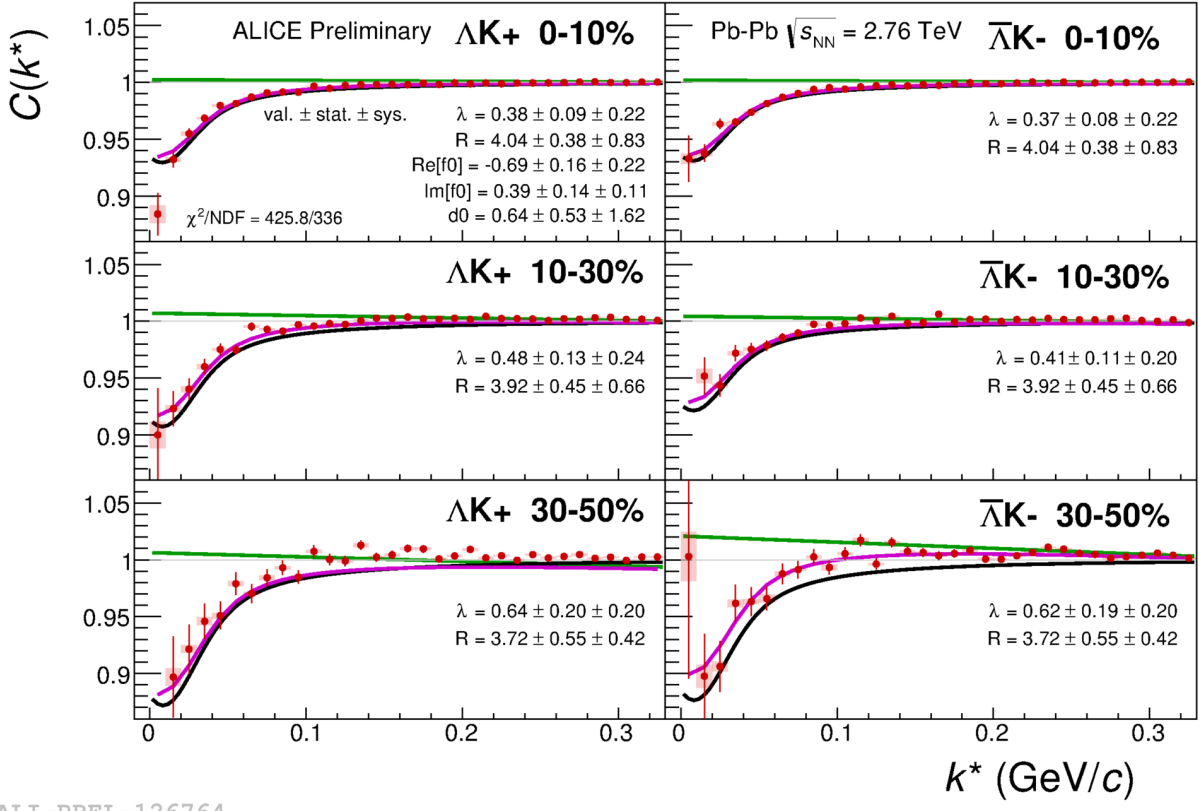


**Fig. 20:** Same as Fig. 19, but with a wider range of view. Fits to the  $\Lambda K_S^0$  (left) and  $\bar{\Lambda} K_S^0$  (right) data for the centralities 0-10% (top), 10-30% (middle), and 30-50% (bottom). The lines represent the statistical errors, while the boxes represent the systematic errors. Each has unique  $\lambda$  and normalization parameters. The radii are shared amongst like centralities; the scattering parameters ( $\mathbb{R} f_0$ ,  $\mathbb{I} f_0$ ,  $d_0$ ) are shared amongst all. The black solid line represents the “raw” fit, i.e. not corrected for momentum resolution effects nor non-flat background. The green line shows the fit to the non-flat background. The purple points show the fit after momentum resolution and non-flat background corrections have been applied. The initial values of the parameters is listed, as well as the final fit values with uncertainties. Here,  $R$  was restricted to [2.,10.] and  $\Lambda$  was restricted to [0.1,0.8].



ALI-PREL-126764

**Fig. 21:** Fits to the  $\Lambda K^+$  (left) and  $\bar{\Lambda} K^-$  (right) data for the centralities 0-10% (top), 10-30% (middle), and 30-50% (bottom). The lines represent the statistical errors, while the boxes represent the systematic errors. Each has unique  $\lambda$  and normalization parameters. The radii are shared amongst like centralities; the scattering parameters ( $\text{Re}[f_0]$ ,  $\text{Im}[f_0]$ ,  $d_0$ ) are shared amongst all. The black solid line represents the “raw” fit, i.e. not corrected for momentum resolution effects nor non-flat background. The green line shows the fit to the non-flat background. The purple points show the fit after momentum resolution and non-flat background corrections have been applied. The initial values of the parameters is listed, as well as the final fit values with uncertainties.

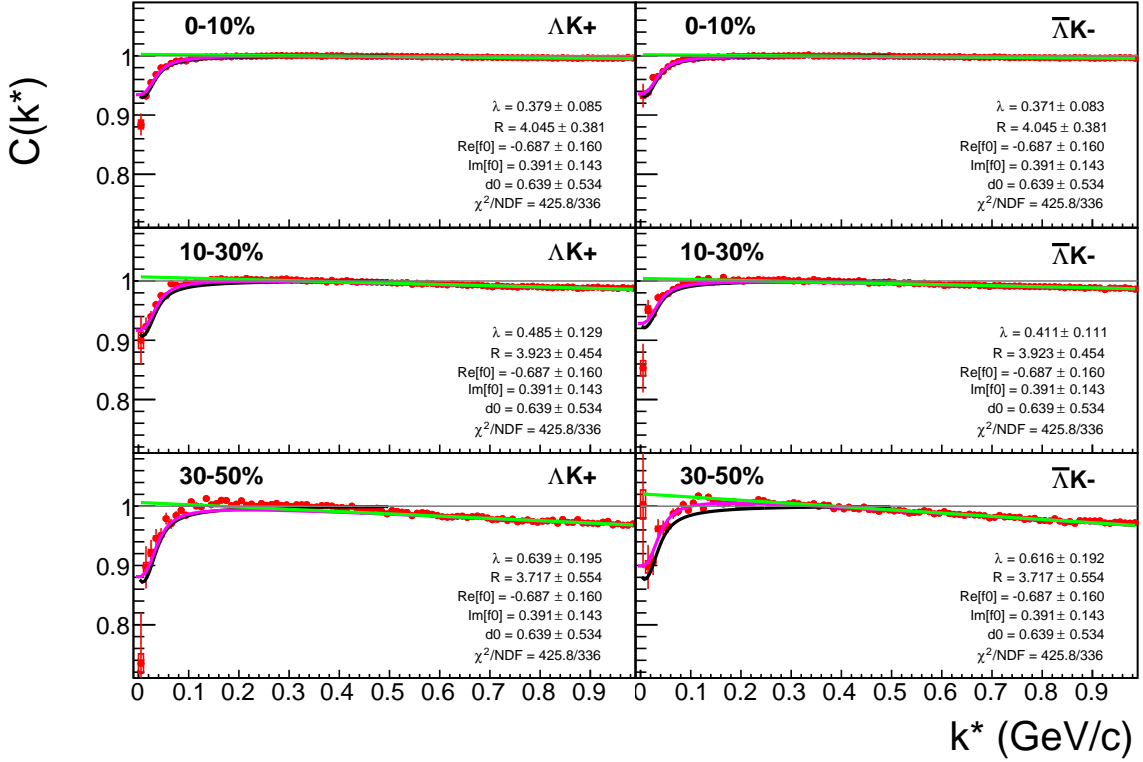


**Fig. 22:** Same as Fig. 21, but with a wider range of view. Fits to the  $\Lambda K^+$  (left) and  $\bar{\Lambda} K^-$  (right) data for the centralities 0-10% (top), 10-30% (middle), and 30-50% (bottom). The lines represent the statistical errors, while the boxes represent the systematic errors. Each has unique  $\lambda$  and normalization parameters. The radii are shared amongst like centralities; the scattering parameters ( $\mathbb{R} f_0$ ,  $\mathbb{I} f_0$ ,  $d_0$ ) are shared amongst all. The black solid line represents the “raw” fit, i.e. not corrected for momentum resolution effects nor non-flat background. The green line shows the fit to the non-flat background. The purple points show the fit after momentum resolution and non-flat background corrections have been applied. The initial values of the parameters is listed, as well as the final fit values with uncertainties.

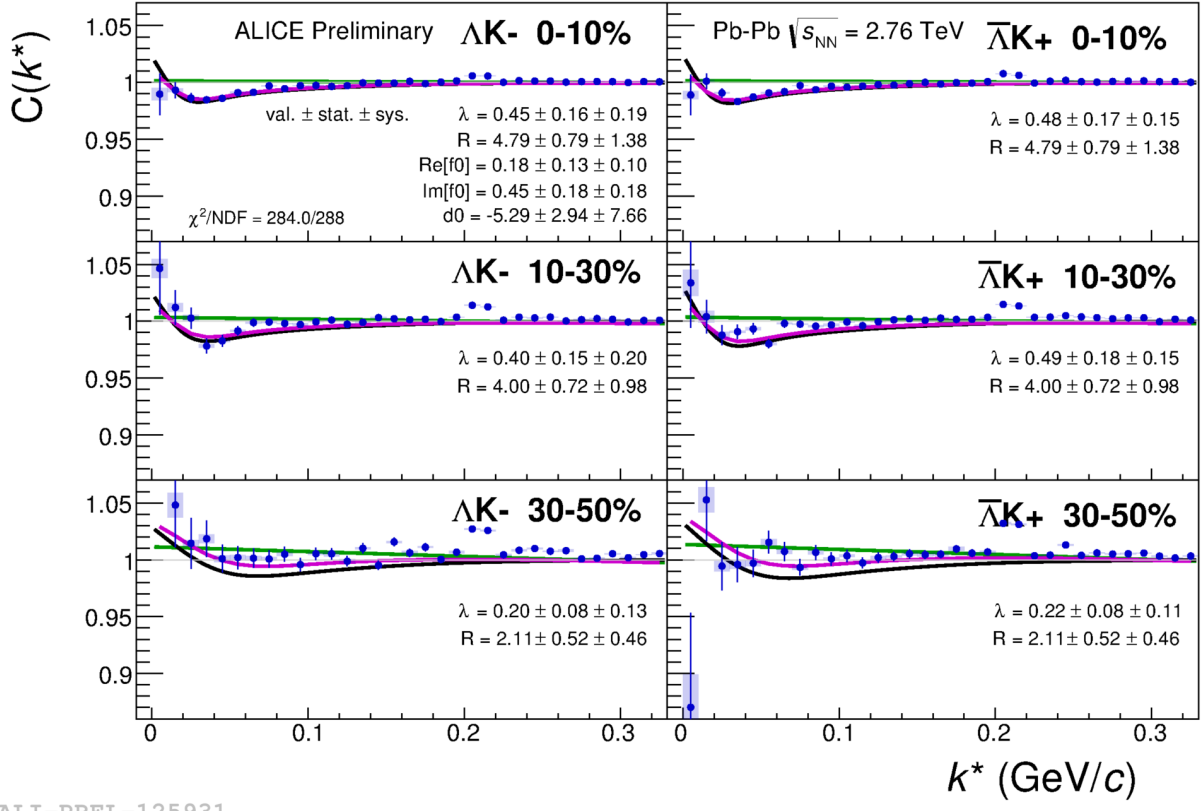


**Fig. 23:** Fits to the  $\Lambda K^-$  (left) with  $\bar{\Lambda} K^+$  (right) data for the centralities 0-10% (top), 10-30% (middle), and 30-50% (bottom). The lines represent the statistical errors, while the boxes represent the systematic errors. Each has unique  $\lambda$  and normalization parameters. The radii are shared amongst like centralities; the scattering parameters ( $Re[f_0]$ ,  $Im[f_0]$ ,  $d_0$ ) are shared amongst all. The black solid line represents the “raw” fit, i.e. not corrected for momentum resolution effects nor non-flat background. The green line shows the fit to the non-flat background. The purple points show the fit after momentum resolution and non-flat background corrections have been applied. The initial values of the parameters is listed, as well as the final fit values with uncertainties.

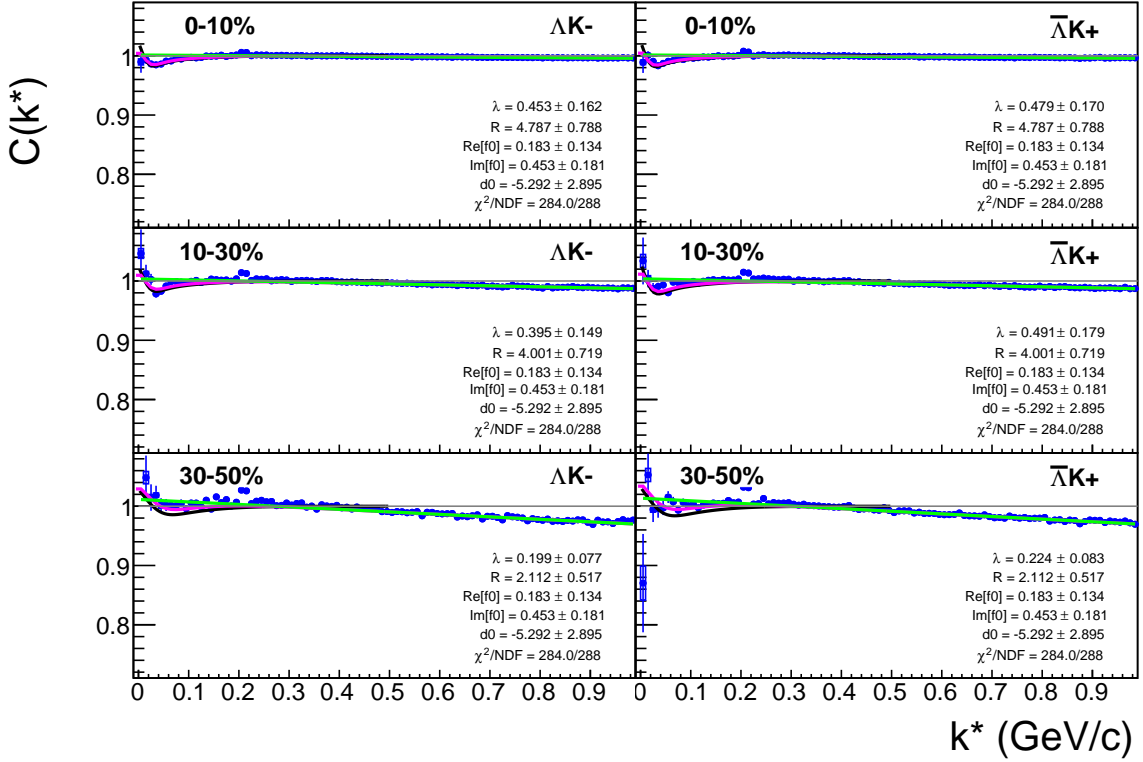


**Fig. 24:** Same as Fig. 23, but with a wider range of view. Fits to the  $\Lambda K^-$  (left) with  $\bar{\Lambda} K^+$  (right) data for the centralities 0-10% (top), 10-30% (middle), and 30-50% (bottom). The lines represent the statistical errors, while the boxes represent the systematic errors. Each has unique  $\lambda$  and normalization parameters. The radii are shared amongst like centralities; the scattering parameters ( $\text{Re}[f_0]$ ,  $\text{Im}[f_0]$ ,  $d_0$ ) are shared amongst all. The black solid line represents the “raw” fit, i.e. not corrected for momentum resolution effects nor non-flat background. The green line shows the fit to the non-flat background. The purple points show the fit after momentum resolution and non-flat background corrections have been applied. The initial values of the parameters is listed, as well as the final fit values with uncertainties.

Fit Results $\Lambda(\bar{\Lambda})K_S^0$						
Pair Type	Centrality	Fit Parameters				
		$\lambda$	$R$	$\mathbb{R}f_0$	$\mathbb{I}f_0$	$d_0$
$\Lambda K_S^0$	0-10%	$0.400 \pm 0.187$ (stat.) $\pm 0.116$ (sys.)	$3.024 \pm 0.541$ (stat.) $\pm 0.329$ (sys.)	$-0.157 \pm 0.031$ (stat.) $\pm 0.043$ (sys.)	$0.176 \pm 0.077$ (stat.) $\pm 0.059$ (sys.)	$3.566 \pm 0.947$ (stat.) $\pm 2.836$ (sys.)
	10-30%		$2.270 \pm 0.413$ (stat.) $\pm 0.324$ (sys.)			
	30-50%		$1.669 \pm 0.307$ (stat.) $\pm 0.280$ (sys.)			
$\bar{\Lambda} K_S^0$	0-10%	$0.400 \pm 0.187$ (stat.) $\pm 0.116$ (sys.)	$3.024 \pm 0.541$ (stat.) $\pm 0.329$ (sys.)	$-0.157 \pm 0.031$ (stat.) $\pm 0.043$ (sys.)	$0.176 \pm 0.077$ (stat.) $\pm 0.059$ (sys.)	$3.566 \pm 0.947$ (stat.) $\pm 2.836$ (sys.)
	10-30%		$2.270 \pm 0.413$ (stat.) $\pm 0.324$ (sys.)			
	30-50%		$1.669 \pm 0.307$ (stat.) $\pm 0.280$ (sys.)			

**Table 1:** Fit Results  $\Lambda(\bar{\Lambda})K_S^0$ . Each pair is fit simultaneously with its conjugate (ie.  $\Lambda K_S^0$  with  $\bar{\Lambda} K_S^0$ ) across all centralities (0-10%, 10-30%, 30-50%), for a total of 6 simultaneous analyses in the fit. Each analysis has a unique  $\lambda$  and normalization parameter. The radii are shared between analyses of like centrality, as these should have similar source sizes. The scattering parameters ( $\mathbb{R}f_0$ ,  $\mathbb{I}f_0$ ,  $d_0$ ) are shared amongst all. The fit is done on the data with only statistical error bars. The errors marked as “stat.” are those returned by MINUIT. The errors marked as “sys.” are those which result from my systematic analysis (as outlined in Section 6).

Fit Results $\Lambda(\bar{\Lambda})K^\pm$						
Pair Type	Centrality	Fit Parameters				
		$\lambda$	$R$	$\mathbb{R}f_0$	$\mathbb{I}f_0$	$d_0$
$\Lambda K^+$	0-10%	$0.379 \pm 0.085$ (stat.) $\pm 0.220$ (sys.)	$4.045 \pm 0.381$ (stat.) $\pm 0.830$ (sys.)	$-0.687 \pm 0.160$ (stat.) $\pm 0.223$ (sys.)	$0.391 \pm 0.143$ (stat.) $\pm 0.111$ (sys.)	$0.639 \pm 0.534$ (stat.) $\pm 1.621$ (sys.)
	10-30%	$0.485 \pm 0.129$ (stat.) $\pm 0.241$ (sys.)	$3.923 \pm 0.454$ (stat.) $\pm 0.663$ (sys.)			
	30-50%	$0.639 \pm 0.195$ (stat.) $\pm 0.204$ (sys.)	$3.717 \pm 0.554$ (stat.) $\pm 0.420$ (sys.)			
$\bar{\Lambda} K^-$	0-10%	$0.371 \pm 0.083$ (stat.) $\pm 0.217$ (sys.)	$4.045 \pm 0.381$ (stat.) $\pm 0.830$ (sys.)	$0.183 \pm 0.134$ (stat.) $\pm 0.095$ (sys.)	$0.453 \pm 0.181$ (stat.) $\pm 0.184$ (sys.)	$-5.292 \pm 2.895$ (stat.) $\pm 7.658$ (sys.)
	10-30%	$0.411 \pm 0.111$ (stat.) $\pm 0.201$ (sys.)	$3.923 \pm 0.454$ (stat.) $\pm 0.663$ (sys.)			
	30-50%	$0.616 \pm 0.192$ (stat.) $\pm 0.203$ (sys.)	$3.717 \pm 0.554$ (stat.) $\pm 0.420$ (sys.)			
$\Lambda K^-$	0-10%	$0.453 \pm 0.162$ (stat.) $\pm 0.186$ (sys.)	$4.787 \pm 0.788$ (stat.) $\pm 1.375$ (sys.)	$0.183 \pm 0.134$ (stat.) $\pm 0.095$ (sys.)	$0.453 \pm 0.181$ (stat.) $\pm 0.184$ (sys.)	$-5.292 \pm 2.895$ (stat.) $\pm 7.658$ (sys.)
	10-30%	$0.395 \pm 0.149$ (stat.) $\pm 0.198$ (sys.)	$4.001 \pm 0.719$ (stat.) $\pm 0.978$ (sys.)			
	30-50%	$0.199 \pm 0.077$ (stat.) $\pm 0.132$ (sys.)	$2.112 \pm 0.517$ (stat.) $\pm 0.457$ (sys.)			
$\bar{\Lambda} K^+$	0-10%	$0.479 \pm 0.170$ (stat.) $\pm 0.152$ (sys.)	$4.787 \pm 0.788$ (stat.) $\pm 1.375$ (sys.)	$0.183 \pm 0.134$ (stat.) $\pm 0.095$ (sys.)	$0.453 \pm 0.181$ (stat.) $\pm 0.184$ (sys.)	$-5.292 \pm 2.895$ (stat.) $\pm 7.658$ (sys.)
	10-30%	$0.491 \pm 0.179$ (stat.) $\pm 0.148$ (sys.)	$4.001 \pm 0.719$ (stat.) $\pm 0.978$ (sys.)			
	30-50%	$0.224 \pm 0.083$ (stat.) $\pm 0.106$ (sys.)	$2.112 \pm 0.517$ (stat.) $\pm 0.457$ (sys.)			

**Table 2:** Fit Results  $\Lambda(\bar{\Lambda})K^\pm$  Each pair is fit simultaneously with its conjugate (ie.  $\Lambda K^+$  with  $\bar{\Lambda} K^-$  and  $\Lambda K^-$  with  $\bar{\Lambda} K^+$ ) across all centralities (0-10%, 10-30%, 30-50%), for a total of 6 simultaneous analyses in the fit. Each analysis has a unique  $\lambda$  and normalization parameter. The radii are shared between analyses of like centrality, as these should have similar source sizes. The scattering parameters ( $\mathbb{R}f_0$ ,  $\mathbb{I}f_0$ ,  $d_0$ ) are shared amongst all. The fit is done on the data with only statistical error bars. The errors marked as “stat.” are those returned by MINUIT. The errors marked as “sys.” are those which result from my systematic analysis (as outlined in Section 6).

**Fit Parameters (value  $\pm$  statistical error  $\pm$  systematic error)**

Pair Type	Centrality	R		
		$\Re f_0$	$\Im f_0$	$d_0$
$\Lambda K^+ & \bar{\Lambda} K^-$	0-10%		<b><math>4.04 \pm 0.38 \pm 0.83</math></b>	
	10-30%		<b><math>3.92 \pm 0.45 \pm 0.66</math></b>	
	30-50%		<b><math>3.72 \pm 0.55 \pm 0.42</math></b>	
		<b><math>-0.69 \pm 0.16 \pm 0.22</math></b>	<b><math>0.39 \pm 0.14 \pm 0.11</math></b>	<b><math>0.64 \pm 0.53 \pm 1.62</math></b>
$\Lambda K^- & \bar{\Lambda} K^+$	0-10%		<b><math>4.79 \pm 0.79 \pm 1.38</math></b>	
	10-30%		<b><math>4.00 \pm 0.72 \pm 0.98</math></b>	
	30-50%		<b><math>2.11 \pm 0.52 \pm 0.46</math></b>	
		<b><math>0.18 \pm 0.13 \pm 0.10</math></b>	<b><math>0.45 \pm 0.18 \pm 0.18</math></b>	<b><math>-5.29 \pm 2.94 \pm 7.66</math></b>
$\Lambda K_S^0 & \bar{\Lambda} K_S^0$	0-10%		<b><math>3.02 \pm 0.54 \pm 0.33</math></b>	
	10-30%		<b><math>2.27 \pm 0.41 \pm 0.32</math></b>	
	30-50%		<b><math>1.67 \pm 0.30 \pm 0.28</math></b>	
		<b><math>-0.16 \pm 0.03 \pm 0.04</math></b>	<b><math>0.18 \pm 0.08 \pm 0.06</math></b>	<b><math>3.57 \pm 0.95 \pm 2.84</math></b>

Figure 25 shows extracted  $R_{\text{inv}}$  parameters as a function of transverse mass ( $m_T$ ) for various pair systems over several centralities. The published ALICE data [6] is shown with transparent, open symbols. The new AK results are shown with opaque, filled symbols. The radii show an increasing size with increasing centrality, as is expected from the simple geometric picture of the collisions. The radii decrease in size with increasing  $m_T$ , and we see an approximate scaling of the radii with transverse mass, as is expected in the presence of collective flow in the system.

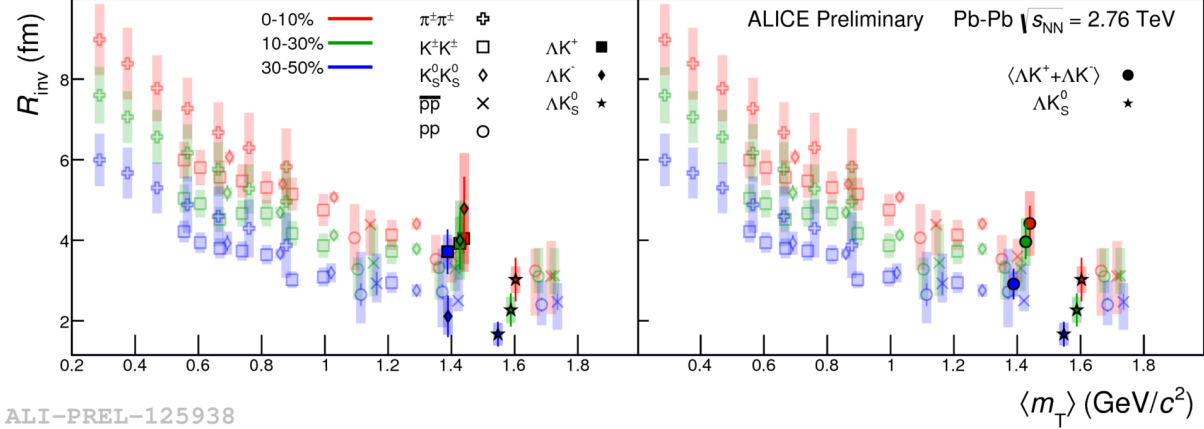


**Fig. 25:** Extracted fit  $R_{\text{inv}}$  parameters as a function of pair transverse mass ( $m_T$ ) for various pair systems over several centralities. The ALICE published data [6] is shown with transparent, open symbols. The new AK results are shown with opaque, filled symbols. In the left, the  $\Lambda K^+$  (with its conjugate pair) results are shown separately from the  $\Lambda K^-$  (with its conjugate pair) results. In the right, all  $\Lambda K^\pm$  results are averaged.

## 7.2 Results: $\Xi K^\pm$

Even without any fits to the data, the fact that the  $\Xi^- K^+$  data dips below unity (Fig. 26) is exciting, as this cannot occur purely from a Coulomb interaction. We hope that this dip signifies that we are able to peer through the overwhelming contribution from the Coulomb interaction to see the effects arising from the strong interaction.

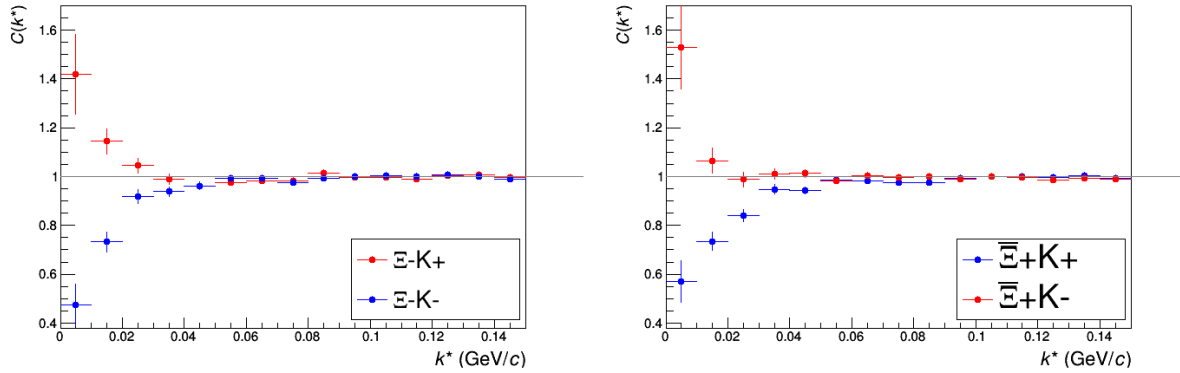


**Fig. 26:**  $\Xi K^\pm$  Results for 0-10% Centrality. (Left)  $\Xi^- K^+$  and  $\Xi^- K^-$  (Right)  $\Xi^+ K^+$  and  $\Xi^+ K^-$

Figure 27 demonstrates graphically, that the  $\Xi^- K^+$  results cannot be described by solely the Coulomb interaction. In this figure, we present the data along with a Coulomb-only band. The Coulomb-only band is spanned by two Coulomb-only curves, whose parameters are given in the figure. The Coulomb-only curves were generated using a technique identical to the generation of the fit function, described in Sec. 5.2, except, of course, with the nuclear scattering parameters all set to zero. The Coulomb-only

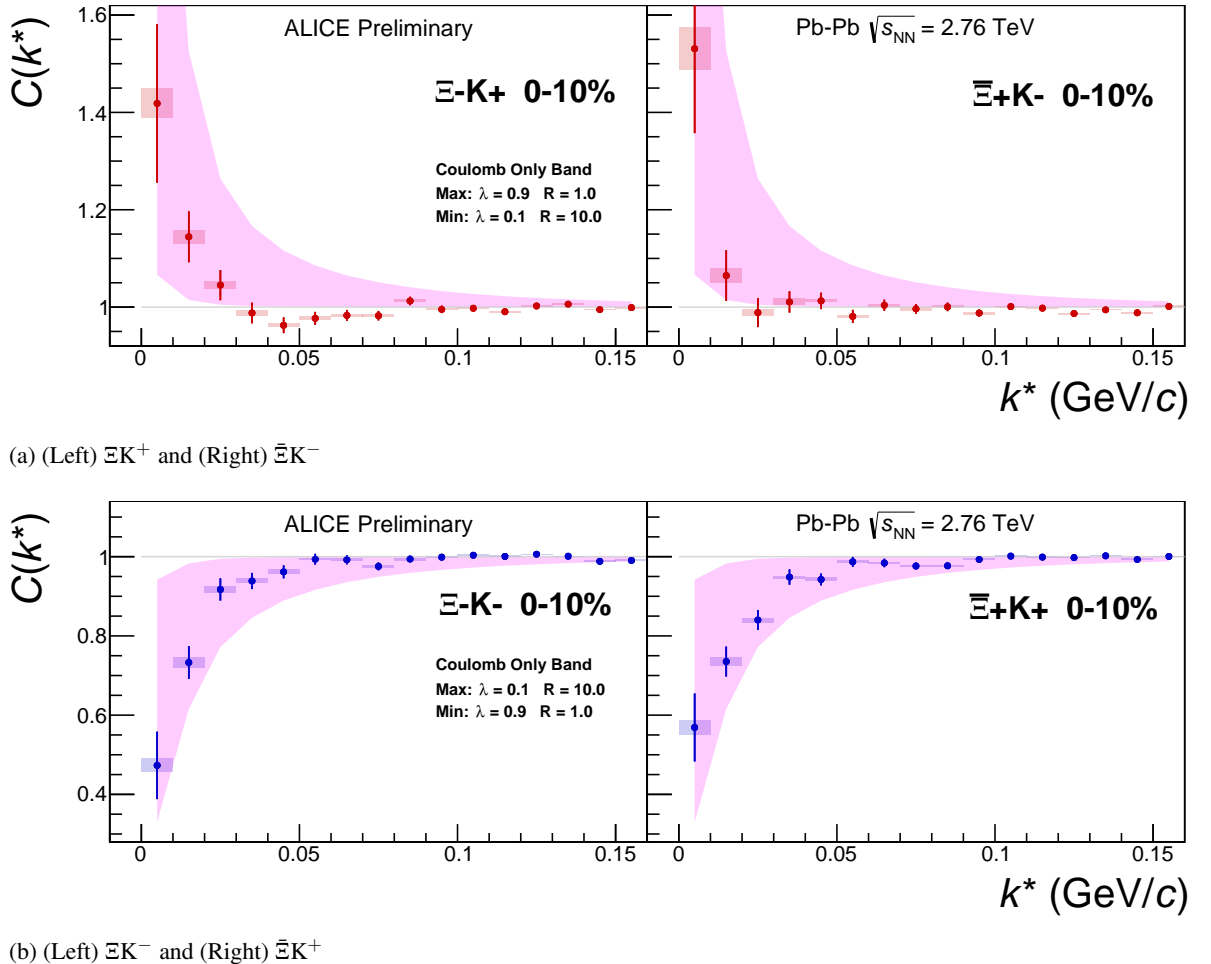


**Fig. 27:**  $\Xi K^\pm$  data with Coulomb-only bands for the 0-10% centrality bin. The Coulomb-only bands span two sets of Coulomb-only curves: (1)  $\lambda = 0.9$ ,  $R = 1.0$  fm and (2)  $\lambda = 0.1$ ,  $R = 10.0$  fm. The Coulomb-only curves are simulated correlation functions for the respective pair system assuming only a Coulomb interaction, i.e. ignoring the strong interaction. The Coulomb-only curves change monotonically with varying  $\lambda$  and varying  $R$ , therefore, any intermediate parameter set will fall within this Coulomb-only band.

577 curves change monotonically with varying  $\lambda$  or varyin radius parametres, therefore, any curves built with  
578 parameter sets intermediate to those use in the Coulomb-only band will be contained in the band.

579 Including the strong interaction into the simulation can dramatically change the resulting correlation  
580 function, as shown in Figure 28. In the figure, the solid line represents a Coulomb-only curve, i.e. a  
581 simulated correlation function with the strong interaction turned off. The dashed lines represent a full  
582 simulation, including both the strong and Coulomb interactions. The two dashed lines differ only in the  
583 real part of the assumed scattering length: positive in Set 1, and negative in Set 2. In the top figure,  
584 for the  $\Xi^- K^+$  simulation, we see that parameter set 2, with a negative real part of the scattering length,  
585 causes the simulated curve to dip below unity, as is seen in the data. If there is a parallel to be drawn  
586 between this analysis and the  $\Lambda K$  analysis, we expect to see similar effects in the  $\Lambda K^+$  system and the  
587  $\Xi^- K^+$  systems. In these systems, we could have an  $s\bar{s}$  annihilation picture. Or, another possible way of  
588 thinking about these systems is in terms of net strangeness. The  $\Lambda K^+$  system has  $S=0$ , while the  $\Lambda K^-$   
589 has  $S=-2$ . The  $\Xi^- K^+$  has  $S=-1$ , while the  $\Xi^- K^-$  has  $S=-3$ .

590 The author was asked to perform a global Coulomb-only fit to the data, to ensure that the system truly  
591 could not be described simply by the Coulomb interaction. In order words, in the fit, the strong force was  
592 turned off, and the  $\Xi^- K^+$ ,  $\bar{\Xi}^+ K^-$ ,  $\Xi^- K^-$ ,  $\bar{\Xi}^+ K^+$  systems all share one sinlge radius parameter, while the

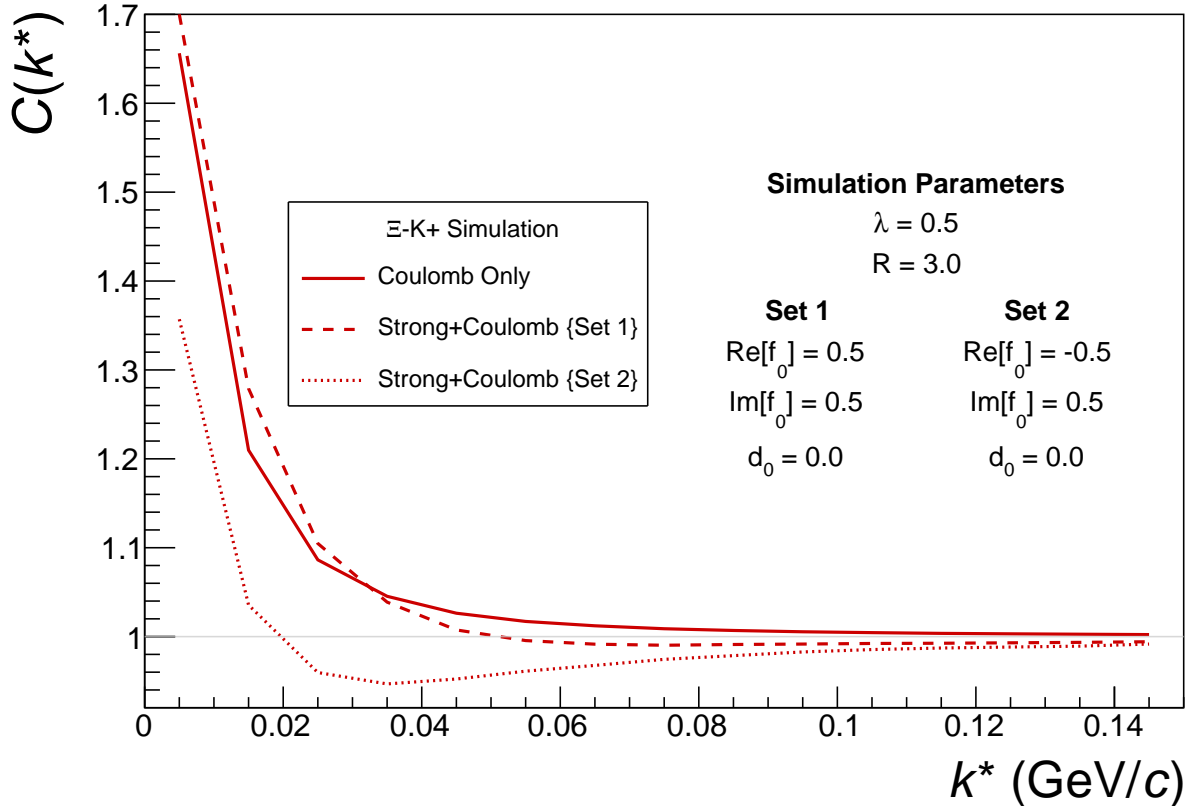
pair and conjugate pair systems share a  $\lambda$  parameter. The results of this fit are shown in Figures 29 and 30. In Fig. 29, there was a lower limit of 0.1 fm placed on the radius parameter, and the radius parameter was initialized to 3 fm (as seems reasonable, when considering the transverse mass of the system and looking at Fig. 25). As is shown in the results, the radius parameter reached this unrealistic lower bound of 0.1 fm. In Fig. 30, the parameters were all unbounded, and the radius parameter was initialized to 10 fm. In this case, the radius parameters reamins high, and ends at an unrealistic value of 10.84 fm. In both cases, the  $\lambda$  parameters are too low. From these figures, we conclude that a global Coulomb-only fit is not suitable for the data.

Although the global Coulomb-only fit failed, it is possible that a Coulomb-only fit performed on  $\Xi^- K^+$  and  $\bar{\Xi}^+ K^-$  separately from  $\Xi^- K^-$  and  $\bar{\Xi}^+ K^+$  could be suitable. The result of such fits are shown in Figures 31 and 32. Figure 31, shows that the fit is not able to describe the dip in the  $\Xi^- K^+$  data below unity. Of course, this is obviously true for an attractive Coulomb-only fit. The radius parameter of 8.43 fm extracted from this fit is unrealistically large. In Figure 32 shows the Coulomb-only fit can described the  $\Xi^- K^-$  data reasonable well; although the extracted radius of 3.73 fm is somewhat larger than expected.

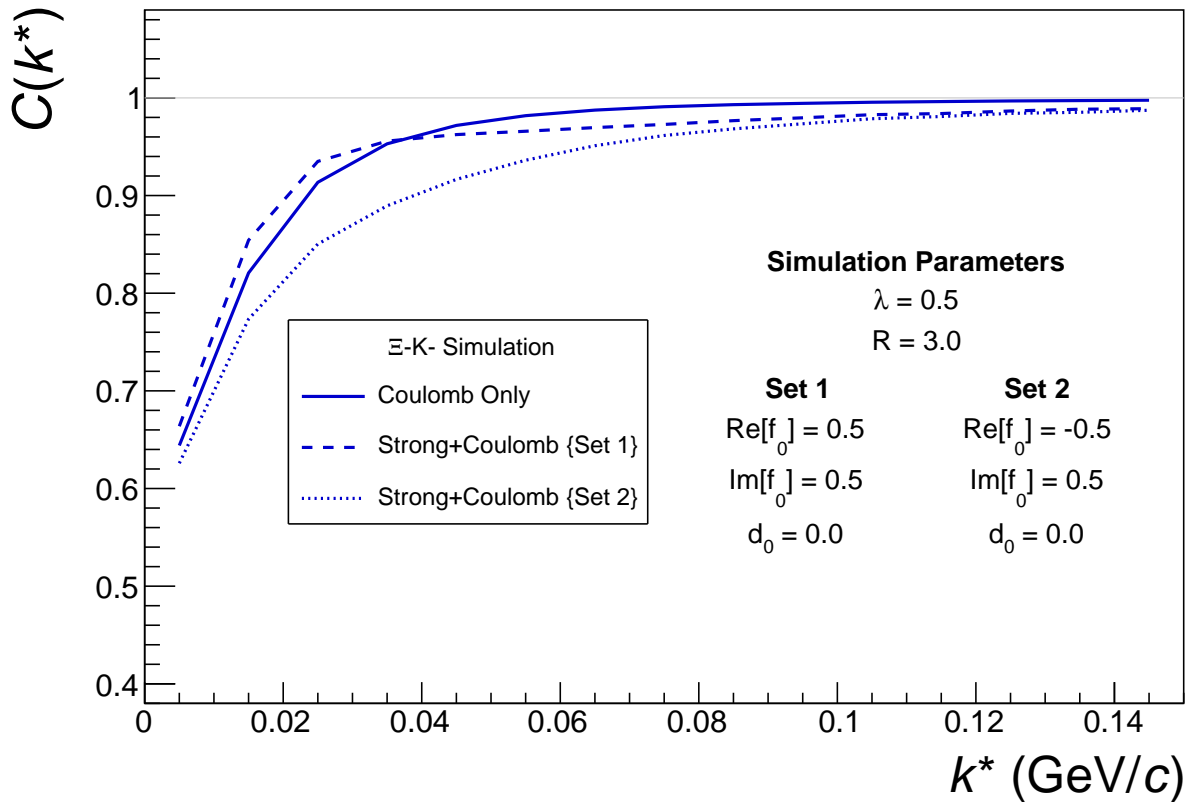
## 8 To Do

### References

- [1] R. Lednicky and V. L. Lyuboshitz. *Sov. J. Nucl. Phys.*, 35:770, 1982.
- [2] Michael Annan Lisa, Scott Pratt, Ron Soltz, and Urs Wiedemann. Femtoscopy in relativistic heavy ion collisions. *Ann. Rev. Nucl. Part. Sci.*, 55:357–402, 2005.
- [3] S. E. Koonin. Proton Pictures of High-Energy Nuclear Collisions. *Phys. Lett.*, B70:43–47, 1977.
- [4] S. Pratt, T. Csorgo, and J. Zimanyi. Detailed predictions for two pion correlations in ultrarelativistic heavy ion collisions. *Phys. Rev.*, C42:2646–2652, 1990.
- [5] Richard Lednicky. Finite-size effects on two-particle production in continuous and discrete spectrum. *Phys. Part. Nucl.*, 40:307–352, 2009.
- [6] Jaroslav Adam et al. One-dimensional pion, kaon, and proton femtoscopy in Pb-Pb collisions at  $\sqrt{s_{NN}} = 2.76$  TeV. *Phys. Rev.*, C92(5):054908, 2015.



(a)  $\Xi K^+$  and  $\bar{\Xi} K^-$  simulation



(b)  $\Xi K^-$  and  $\bar{\Xi} K^+$  simulation

**Fig. 28:** Effect on the Coulomb-only curve of including the strong interaction for  $\Xi K^\pm$  systems. The solid line represents a Coulomb-only curve, i.e. a simulated correlation function with the strong interaction turned off. The dashed lines represent a full simulation, including both the strong and Coulomb interactions. The two dashed lines differ only in the real part of the assumed scattering length: positive in Set 1, and negative in Set 2.

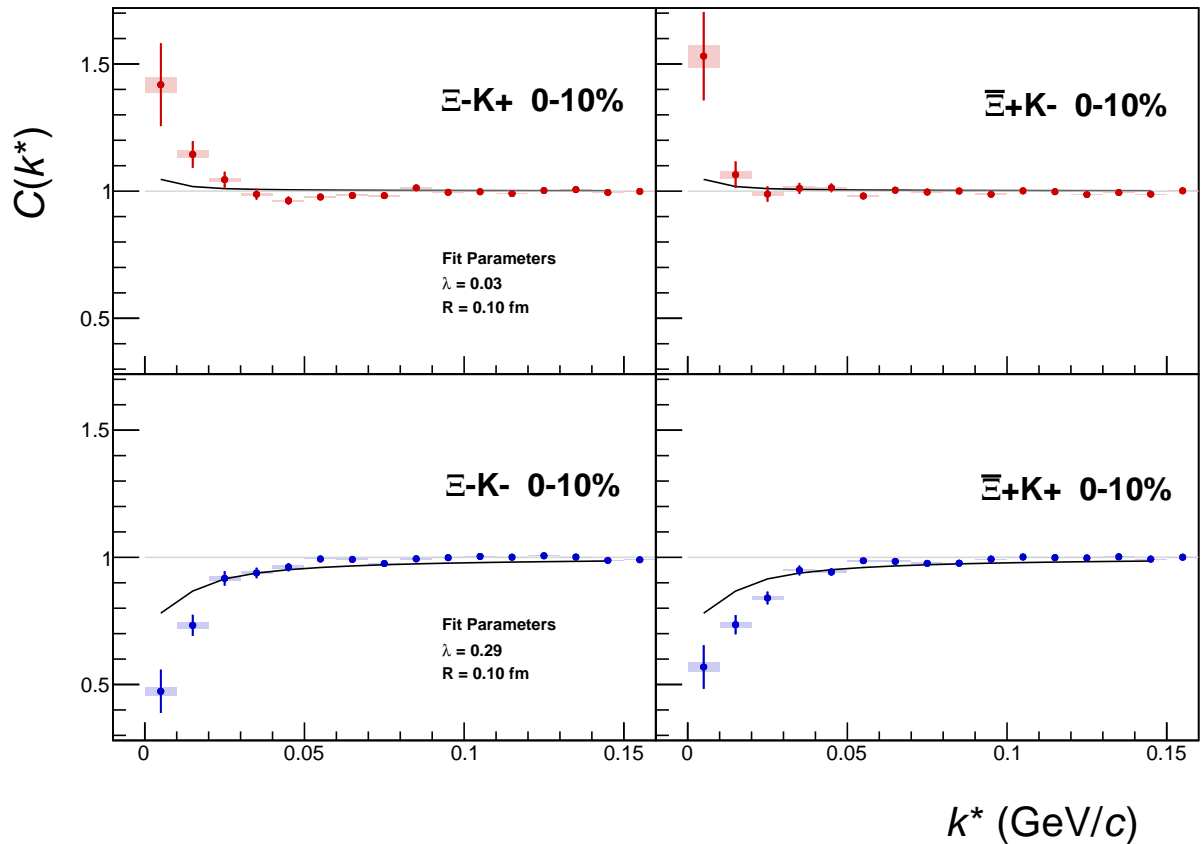


**Fig. 29:**  $\Xi K^\pm$  Global Coulomb-only fit (Set 1) for 0-10% centrality. In this fit, there was a lower limit of 0.1 fm placed on the radius parameter, and the radius parameter was initialized to 3 fm (as seems reasonable, when considering the transverse mass of the system and looking at Fig. 25). As is shown in the results, the radius parameter reached this unrealistic lower bound of 0.1 fm. Also, the extracted  $\lambda$  parameters are too low.

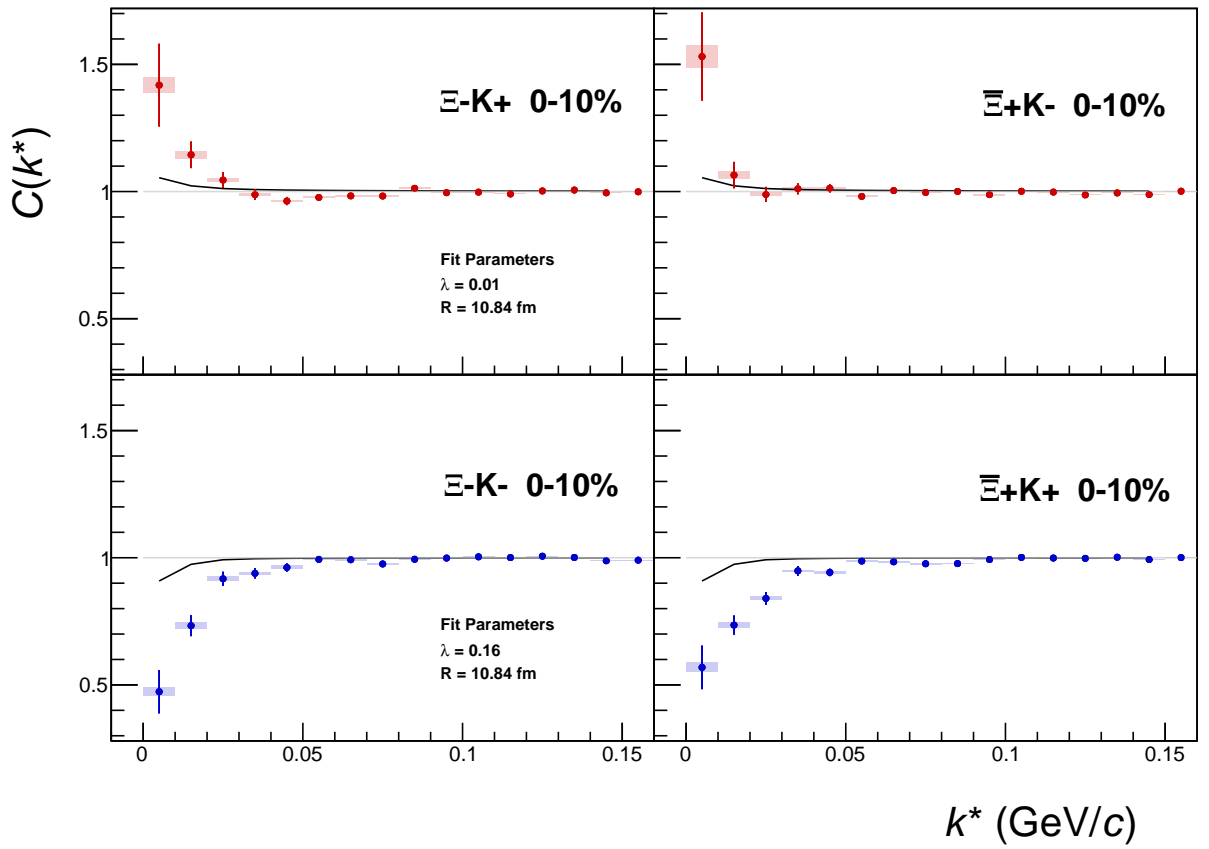


**Fig. 30:**  $\Xi K^\pm$  Global Coulomb-only fit (Set 2) for 0-10% centrality. In this fit, the parameters were all unbounded, and the radius parameter was initialized to 10 fm. In this case, the radius parameters remain high, and ends at an unrealistic value of 10.84 fm. Also, the extracted  $\lambda$  parameters are too low.

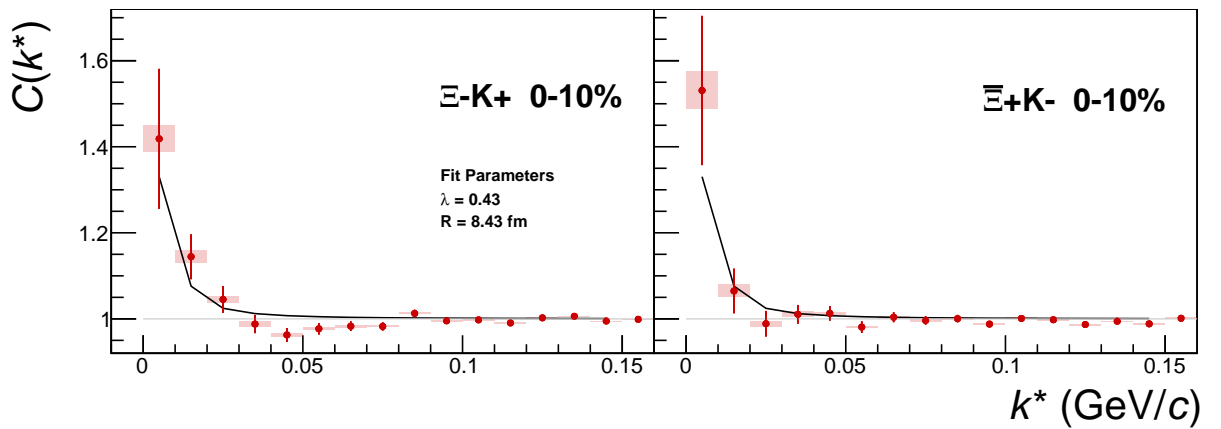


**Fig. 31:**  $\Xi^- K^+$  Coulomb-only fit for 0-10% centrality

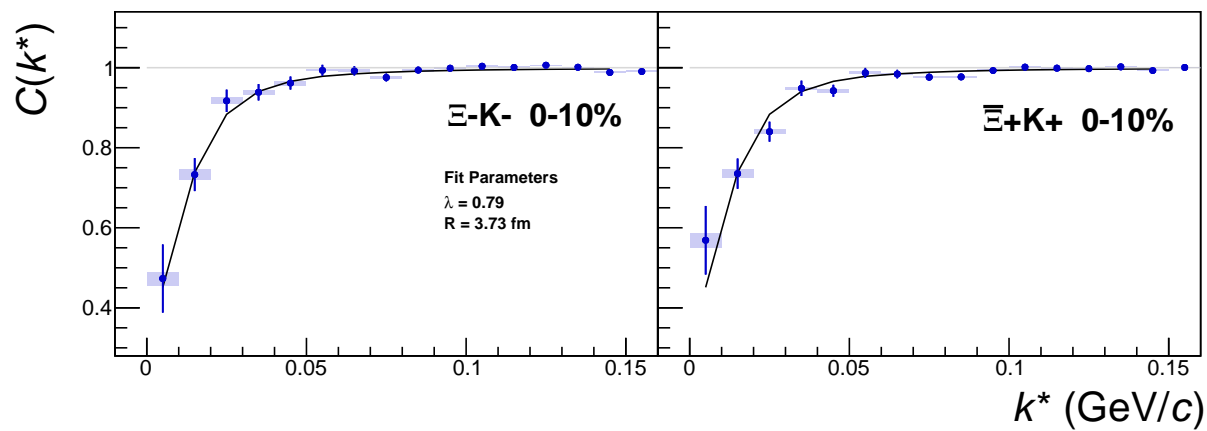


**Fig. 32:**  $\Xi^- \text{K}^-$  Coulomb-only fit for 0-10% centrality